Supporting Information

Elucidating Performance Degradation Mechanisms in Non-Fullerene Acceptor Solar Cells

Vinod K. Sangwan,[a,#,] Zachary Martin,[a,#] Guoping Li,[b] Fei Qin,[b] Shreyash Hadke,[a] Robert M. Pankow,[b] Woo Cheol Jeon,[b] Ding Zheng,[b] Yongjoon Cho,[b] Ryan M. Young,[b,*] Kevin L. Kohlstedt,[b,*] Michael R. Wasielewski,[b,*] George C. Schatz,[b,*] Antonio Facchetti,[b,c,*] Mark C. Hersam,[a,b,d,*] and Tobin J. Marks[b,*]*

[a] Department of Materials Science and Engineering, Northwestern University, Evanston, Illinois 60208 (USA)

[b] Department of Chemistry, Northwestern University, Northwestern University, Evanston, Illinois 60208 (USA)

[c] School of Materials Science and Engineering, Georgia Institute of Technology, Atlanta, Georgia 30332 (USA)

[d] Department of Electrical and Computer Engineering, Northwestern University, Evanston, Illinois 60208 (USA)

[#]Equal Contributions

***** Corresponding Authors

V. K. S. (vinod.sangwan@northwestern.edu),

K. L. K. (kkohlstedt@northwestern.edu),

M. R. W. (m-wasielewski@northwestern.edu),

G. C. S. (g-schatz@northwestern.edu),

A. F. (a-facchetti@northwestern.edu),

T. J. M. (t-marks@northwestern.edu),

M. C. H. (m-hersam@northwestern.edu)

Section 1. Sample Fabrication

Organic solar cells (OSCs) were fabricated using the protocols described earlier.[1] The inverted device structure of ITO/ZnO/**PBDB-TF:Y6**/MoO_3/Ag was prepared as follows. First, ITO substrates were cleaned by sonicating sequentially in an aqueous detergent solution, deionized water, methanol, acetone, and isopropanol (20 min each). After drying with an N_2 gun, the ITO substrates were treated with UV/ozone (Jelight Co.) for 15 min. Then, a ZnO layer was spin-coated on ITO substrates at 7000 rpm for 30 s using an acceleration of 8000 rpm/s using a precursor solution of 0.5 mol/L zinc acetate dihydrate and 0.5 mol/L ethanolamine in 2-methoxyethanol. The resulting ZnO film was annealed at 170 °C for 20 min in air. Then the substrates were transferred into an argon-filled inert glovebox for spin-coating of the blend active layer. The active layer solutions were prepared by co-dissolving the donor polymer and acceptor molecules in a chloroform solvent while stirring overnight. The total concentration of the active layer solution was 16 mg/mL with a donor:acceptor (**PBDB-TF:Y6**) ratio of 1:1.2. The mixed solution was spin-coated at 1500 rpm and the active layer was annealed 100 °C for 10 min. The thickness of the active layer was measured to be 120 nm using a profilometer. Finally, a 10-nm-thick MoO_3 and 100-nm-thick Ag were evaporated through a shadow mask at ≈10^{-6} Torr. The calibrated device area is 6.25 mm^2.

Section 2. Electrical Measurements

The performance metrics of solar cells were performed using the protocol described earlier,[1, 2], and current-voltage characteristics were measured under a simulated AM-1.5G irradiation (100 mW cm^{-2}) illumination from the class-AAA Solar Simulator in an argon-filled

glove box. The solar light intensity was calibrated with an NREL-certified monocrystalline Si photodiode. External quantum efficiency (EQE) of OSCs was measured using a Newport QE-PV-SI setup. Incident light from a Xe lamp (300 W) was passed through a monochromator (Newport Cornerstone 260) and focused on the devices housed inside the glove box. The current was measured by using a current pre-amplifier (Newport, 70710QE) and a lock-in amplifier (Newport, 70105 Dual channel Merlin). A Newport 70356 silicon diode was used as a reference for EQE measurements.

Section 3. Temperature-dependent current and capacitance measurements

For temperature-dependent current-voltage (IVT) and thermal admittance spectroscopy (TAS), we used a liquid N_2 cryostat from a Deep Level Transient Spectroscopy (DLTS) setup from Semetrol, LLC. The cryostat chamber is originally built by Advanced Research Systems (ARS) and customized by Semetrol, LLC. The base pressure of 10^{-3} Torr was achieved before cooling down the cold finger. After pouring liquid N_2 down in the cold finger housing, the pressure reached below 10^{-6} Torr due to cryogenic pumping. The sample temperature was controlled by a calibrated heater. Thus, IVT measurements were carried out by using Keithley 2400 source meter that was controlled by a home-built LabVIEW program. TAS measurements were conducted by a Solartron 1260 impedance analyzer using an AC amplitude of 50 mV. OSCs were degraded by exposing OSCs to solar light built into a solar cell analyzer (Class A Spectra-Nova Technologies), equipped with a xenon arc lamp and AM1.5G filter. Sequential degradation was achieved in ambient exposure and as described above, performance metrics were measured in the argon glove box and variable temperature IVT and TAS measurements were carried out in the vacuum. Note, electronics, and software from Semetrol, LLC were not used for any measurements since the in-house measurement setup achieved a lower noise floor.

Section 4. Optical absorption spectroscopy

Optical (UV-Vis-NIR) absorbance spectroscopy was performed on neat **Y6**, neat **PBDB-TF,** and neat **PBDB-TF:Y6** blend films using a Varian Cary 5000 Instrument (Supporting Fig. S9). These films were prepared on ZnO/ITO substrates using the same spin coating condition that we used to make solar cells. All films were subjected to the same degradation protocol as used for Transient Absorption Spectroscopy and GIWAXS measurements, i.e., exposure to AM-1.5G (100 $mW \cdot cm^{-2}$) illumination under ambient conditions for 30 min. Bare ZnO/ITO substrate did not show any noticeable change in absorption spectra after UV exposure and thus was used for background correction for neat **Y6**, neat **PBDB-TF,** and neat **PBDB-TF:Y6** blend films.

Section 5. Integrated Photocurrent Device Analysis

IPDA measurements were carried out by following the protocol outlined earlier.[1-6] Illumination intensities were varied by using neutral density filters in a Thor Labs FW212CNEB filter wheel. Photocurrent ($J_{PC} = J_{light} - J_{dark}$) *versus* effective voltage ($V_{eff} = V_{OC} - V$) measurements were performed using a Keithley 2400 source meter. Impedance measurements were carried out by a Solartron 1260 impedance analyzer operating at an AC amplitude of 100 mV in the frequency range of 100 Hz to 5 MHz. Chemical capacitance (C_μ) was obtained by taking out the depletion capacitance (in the dark at a large negative bias of −2 V) from the total capacitance using an AC amplitude of 100 mV at 1 kHz. The impedance meter was controlled by ZPlot/ZView software from Scribner Associates, Inc. and all equipment was controlled by a homemade Autoit script for full automation of measurement and analysis, as described here,

https://github.com/MikeHeiber/FlexEDMS

Section 6. Transient Absorption Spectroscopy Measurements

Details of the femtosecond (fsTA) and nanosecond (nsTA) transient absorption spectroscopy studies have been described previously.[7] Briefly, the output of a 1 kHz, 1 W, 100 fs Ti:sapphire laser system at 827 nm (Tsunami oscillator and Spitfire amplifier, Spectra-Physics) is split to generate a broadband continuum probe and to pump a non-collinear optical parametric amplifier (TOPAS-Prime, Light-Conversion LLC) tuned to 800 nm, which is then depolarized to suppress orientation-dependent dynamics. The fsTA probe is generated by pumping a rastering CaF_2 crystal (330-850 nm) or a proprietary crystal from Ultrafast Systems (850-1600 nm); the nsTA probe is provided a separately delayed broadband laser system (EOS, Ultrafast Systems). Time-resolved spectra are acquired on a commercial spectrometer (customized Helios-EOS, Ultrafast Systems), where the Helios spectrometer is used for pump-probe delays up to 7.4 ns and the EOS spectrometer is used for pump-probe delays up to 340 μs. The films were measured at room temperature under a vacuum of 10^{-3} Torr to minimize potential sample degradation or quenching of triplet and/or anionic states by exposure to ambient oxygen.

Before kinetic analysis, the fsTA and nsTA data are scatter-subtracted and chirp-corrected, and the visible and NIR data are spectrally merged (Surface Xplorer 4, Ultrafast Systems). The fsTA and nsTA spectra were then merged in the time domain using a program in MATLAB. The kinetic analysis is based on a global fit to selected single-wavelength kinetics and is implemented in MATLAB. Thus, the kinetic data from multiple wavelengths are fit using global analysis. Each wavelength is given an initial amplitude that is representative of the spectral intensity at the initial time t_0. To fit the merged TA data, we used the following sequential kinetic model with six species, A - F.

$$\frac{dA}{dt} = -k_1[A]$$

$$\frac{dB}{dt} = k_1[A] - k_2[B]$$

$$\frac{dC}{dt} = k_2[B] - k_3[C]$$

$$\frac{dD}{dt} = k_3[C] - k_4[D] \qquad \text{Equation S1}$$

$$\frac{dE}{dt} = k_4[D] - k_5[E]$$

$$\frac{dF}{dt} = k_5[E] - k_6[F]$$

Note that this model is an oversimplification and does not account for many-body effects such as singlet-singlet- and triplet-triplet annihilation, both of which are bimolecular. Similarly, this model does not directly capture diffusion processes and the spatially distributed nature of simpler kinetic processes. The simplifications were made to demonstrate the timescales over which the degradations have the strongest effect.

Section 7. GIWAXS Measurements

Grazing-incidence wide-angle x-ray scattering (GIWAXS) measurements were performed at beamline 8ID-E at the Advanced Photon Source at Argonne National Laboratory. The samples were irradiated at incidence angles from 0.130° to 0.140° in a vacuum at 10.915 keV for two summed exposures of 2.5 s each. Signals were collected with a Pilatus 1M detector located at a distance of 228.16 mm from the samples. Blend films for GIWAXS were prepared according to the procedure for photovoltaic device active layers as described above onto pre-cleaned (sonicated in IPA and acetone for 20 min at 50 °C followed by O_2-plasma treatment for 10 min.) Si substrates

with a dimension of 20 mm x 10 mm. All films were prepared in an argon-filled glovebox. GIWAXS data was processed and analyzed using the GIXSGUI software for MATLAB written by Zhang Jiang and available at https://www.aps.anl.gov/Sector-8/8-ID/Operations-and-Schedules/Useful-Links/Sector-8-GIXSGUI. CCL values were obtained using the Scherrer equation: $2\pi K/FWHM$ (where $K = 0.93$).

Section 8. Computational Details

Density functional-based tight binding (DFTB) calculations were carried out using DFTB+ code[8] to investigate frontier molecular orbitals and density of states (DOS). To facilitate faster computations, we selected molecules with alkyl groups shorter than those in the original **Y6** molecule,[1] as energy levels of their frontier molecular orbitals showed only marginal differences compared to the original molecule (Supporting Table S3). And each molecule was hydrogenated after degradation to achieve a neutral charge. All structures were optimized by using third-order parametrization for organic and biological systems (3OB) parameter set[9-11] where D3 dispersion correction[12] was added with Becke-Johnson damping.[13] A convergence tolerance in the self-consistent charge (SCC) cycle was set to 10^{-5}. For the calculation of crystal structures, the k-point set was set to 3×1×2. Images of structures and frontier molecular orbitals were produced using VESTA software.[14] Each energy spectra of the total density of states (TDOS) and partial density of states (PDOS) was smeared with a value of 50 meV.

The UV/vis absorption spectra for each of the fragments was generated using time-dependent density functional theory (TDDFT) using Turbomole.[15] The random-phase approximation (RPA) was used to approximate dispersion interactions of the ground state when applying the excited state perturbation. The excitation spectra were computed with the B3LYP

functional and the def2-TZVP basis set. The TDDFT functional B3LYP was used in order to accurately get a mixture of short-range and long-range interactions between the hole and electron of the exciton. The number of excitations included in the spectra was 100, which was enough to get to excitations below 250 nm.

The natural transition orbitals (NTOs) were calculated from the one-particle transition density orbital solved using the method described in Ref.[16] over the first 100 excited states (n). We show the transitions between 200 nm and 800 nm in Supporting Fig. S36-41 with a broadening of 0.07 eV.

We acknowledge the use of Turbomole: TURBOMOLE V7.7 2022, a development of the University of Karlsruhe and Forschungszentrum Karlsruhe GmbH, 1989-2007, TURBOMOLE GmbH, since 2007; available from https://www.turbomole.org.

Section 9. MALDI-ToF Measurements

The pristine **Y6** samples were prepared by directly depositing as-purchased **Y6** as a chloroform solution onto the MALDI sample plate without any Matrix and then drying. For degraded **Y6**, a ITO/ZnO/**Y6** stack was fabricated by following the same procedure as OSCs (Section 1) so that the same ZnO-activated degradation pathway could be achieved under solar illumination. After illumination for 30 min, degraded ZnO/Y6 film was treated with 1,2-dichlorobenzene (DCB) to extract the organic component, and the resulting solution then deposited onto the MALDI plate without any Matrix and dried. The samples were analyzed with a Bruker Rapiflex MALDI-TOF mass Spectrometer, in Reflector mode, and using Positive Ion polarity. The method used (RP500-4000) had a mass range of 500-4000 amu. The scans were collected by summing 4000 laser shots per scan with a laser firing rate of 1000/second. The Laser power was

attenuated at about 70% to give an intensity of about $2x10^4$ for comparison of data from different spots and scans.

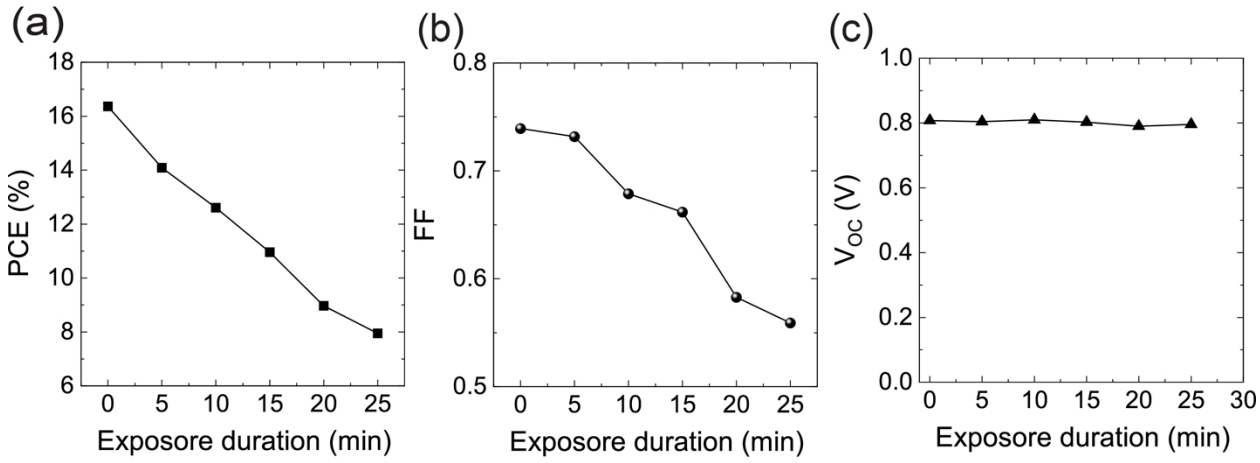

Figure S1. (a), (b), (c) Evolution of OSC PCE, FF, and V_{OC} for **PBDB-TF:Y6** solar cells as a function of exposure to solar illumination, respectively.

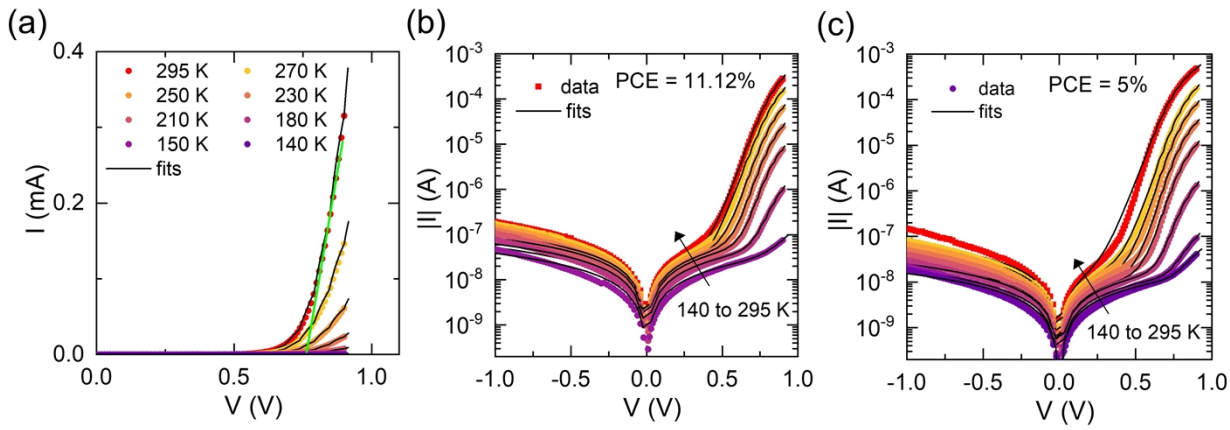

Figure S2. (a) Linear-linear plots of current-voltage (*I-V*) characteristics for a pristine **PBDB-TF:Y6** solar cell from Fig. 1e. The green line shows an onset voltage of 0.77 V at 295 K. The legend in (a) applies to all plots. (b), (c) Log-linear *I-V* curves at different temperatures for degraded cells with PCE of 11.12 % and 5 %, respectively.

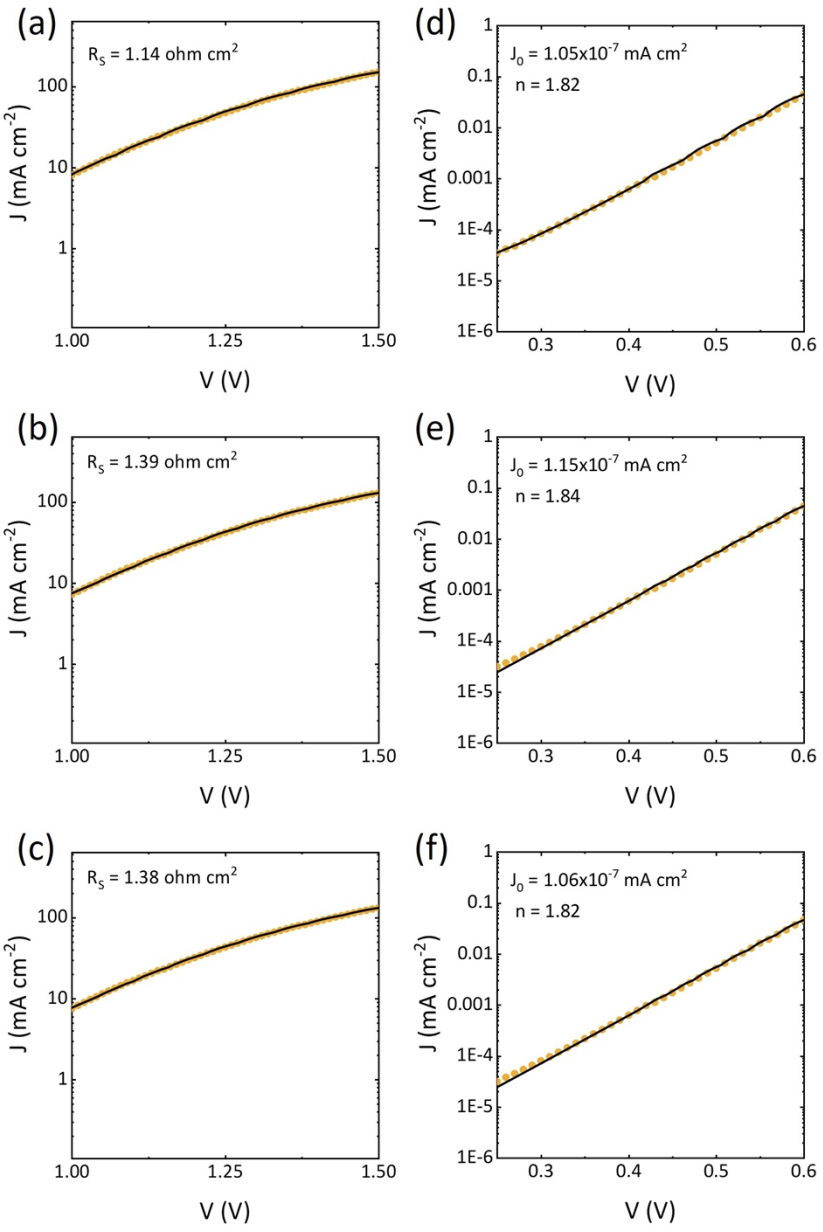

Figure S3. (a)-(c) Current-density (J)-voltage (V) characteristics of three **PBDB-TF:Y6** solar cells measured in the dark up to an applied voltage bias of 1.5 V. The black lines show fits to the generalized Shockley equation (eq. 1 in the main text) at a high voltage range to extract series resistance (R_s) of 1.14-1.38 Ω.cm^2 which is 18.24-22.24 Ω for cells of area = 6.25 mm^2. (d)-(f) The low voltage part of J-V dominated by rectifying behavior is fit to the same equation to extract the reverse saturation current (J_0) and ideality factor (n).

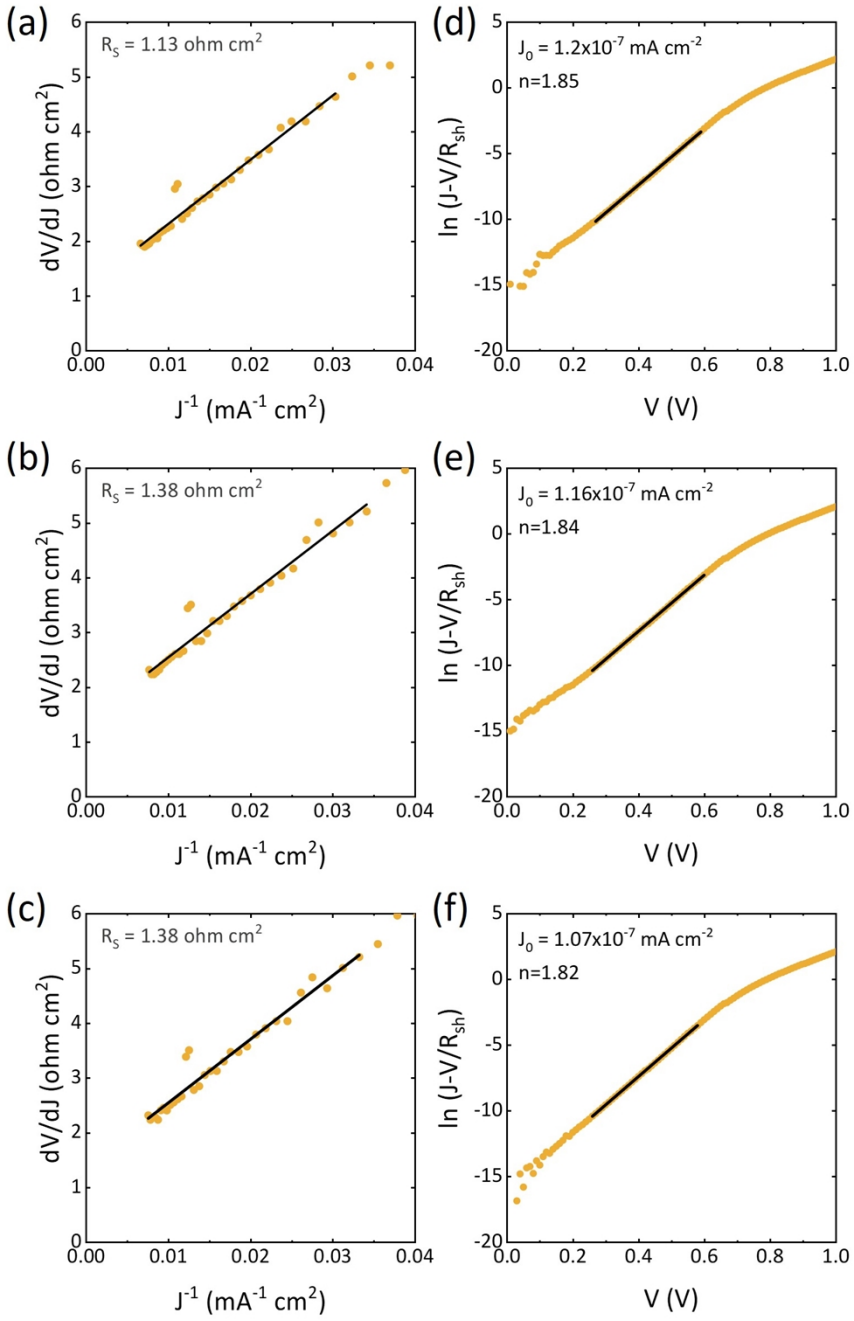

Figure S4. (a)-(c) J-V characteristics of data from Fig. S3 for the same three **PBDB-TF:Y6** solar cells, fit by the Hegedus-Shafarman method in the high voltage range (up to 1.5 V) to extract R_s values that agree with the values obtained in Fig. S3(a)-(c). (d)-(f) The method is used to fit the low voltage part of the JV curves to extract J_0 and n which also agree with values in Fig. S3(d)-(f).

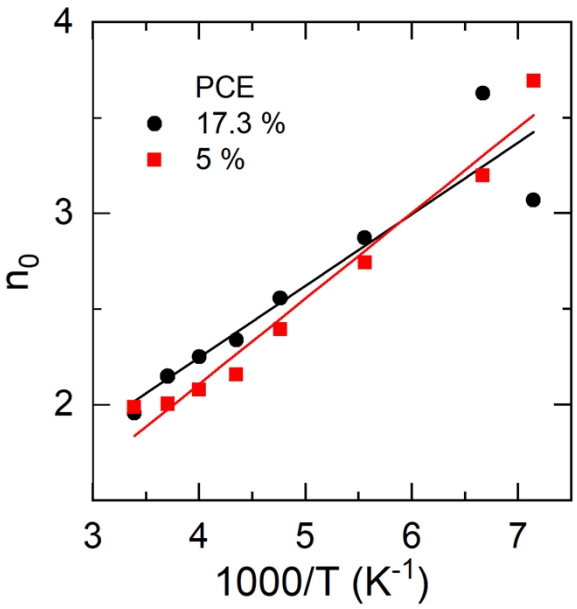

Figure S5. Diode ideality factor (n_0) from generalized non-ideal Shockley equation plotted as a function of 1/T for pristine (PCE = 17.3 %) and degraded (PCE = 5.0 %) **PBDB-TF:Y6** cells resulting in slopes of 0.37 and 0.44, respectively.

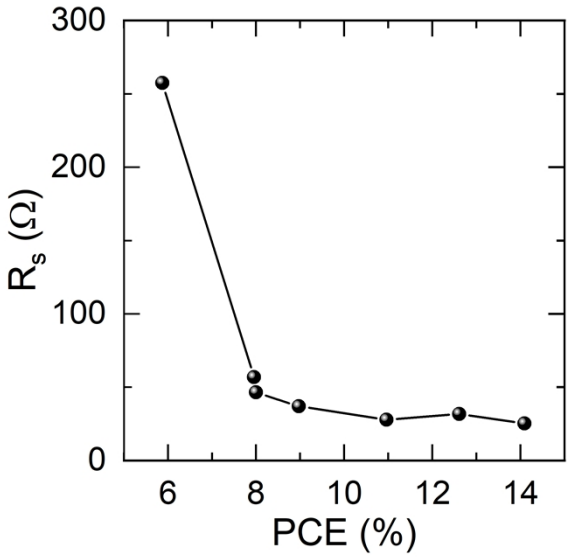

Figure S6. Contact resistance (Rs) extracted from impedance spectroscopy as a function of PCE of **PBDB-TF:Y6** solar cells during degradation.

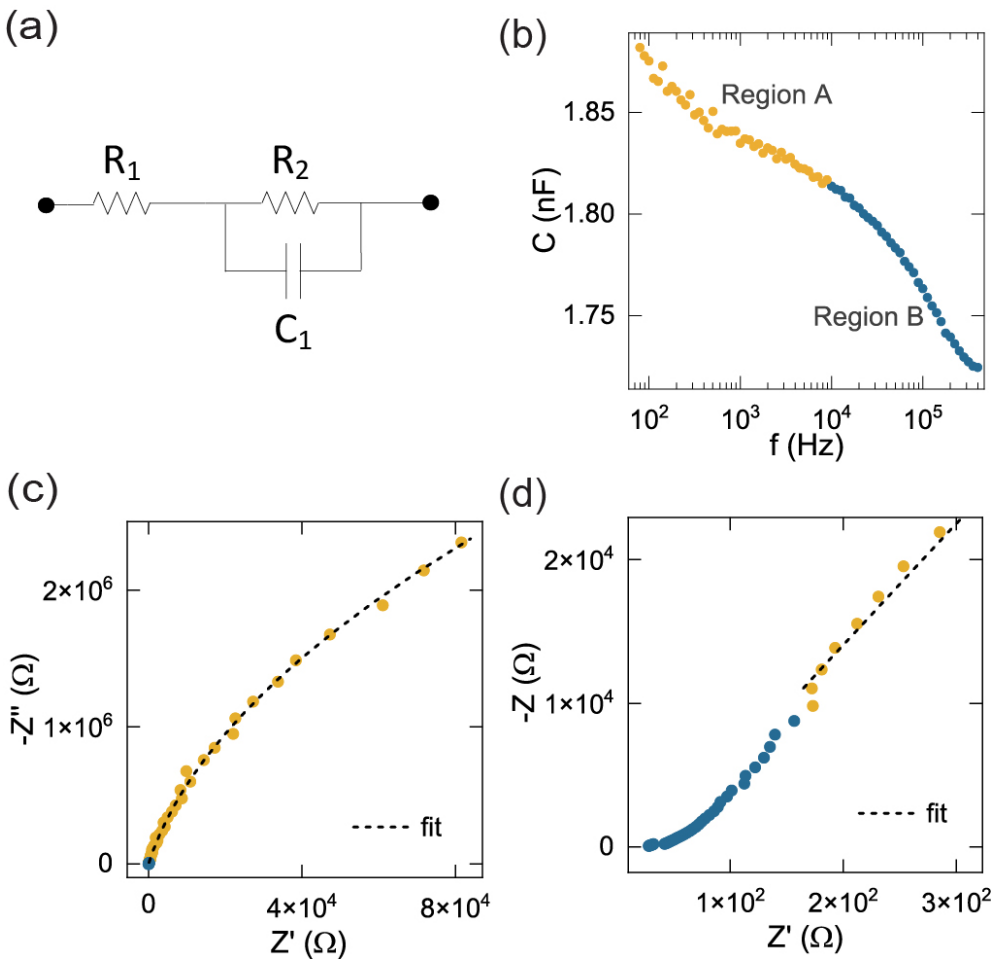

Figure S7. (a) A RC model used for fitting impedance data. (b) Capacitance-frequency (*C-f*) plot of **PBDB-TF: Y6** solar cell at 200 K, showing regions A and B, as described in Fig. 2a. (c) Nyquist plot of the data corresponding to the *C-f* plot, along with fitting of data in Region A using the RC model. (d) Nyquist plot showing that the datapoints corresponding to Region B do not follow the fitting curve of datapoints in Region A, suggesting that using the RC model in this region leads to an artifact of decreasing *C* in the *C-f* curve in Region B. Thus, the capacitance decreases at high frequencies (region B, 10-100 kHz) is not related to trap states, but to the inapplicability of the RC model at these frequencies.

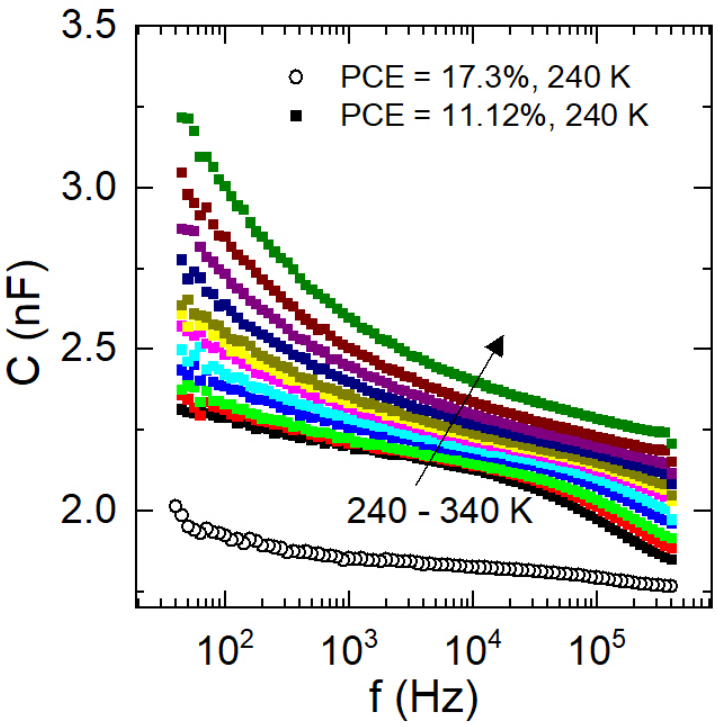

Figure S8. Capacitance-frequency (*C-f*) characteristics of the degraded **PBDB-TF:Y6** solar cell (PCE = 11.1%) at varying temperatures from 240 – 340 K at a step of 10 K. A *C-f* curve for the pristine **PBDB-TF:Y6** solar cell (PCE = 17.2% from Fig. 3a) at 240 K is also shown for comparison.

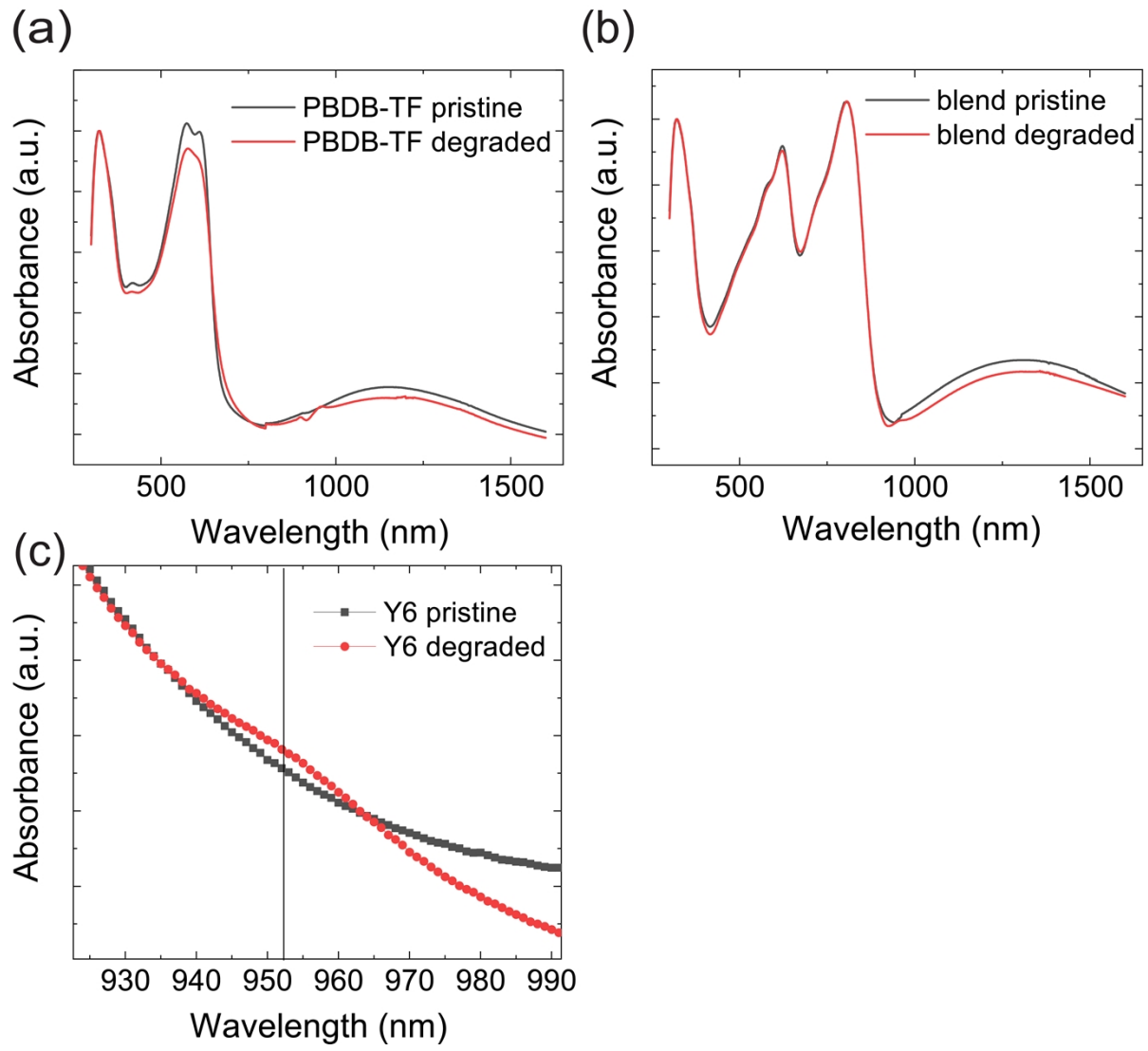

Figure S9. (a), (b) Optical absorbance of a neat **PBDB-TF** and **PBDB-TF:Y6** blend films spin-coated on ZnO/ITO substrate before (pristine) and after exposure (degraded) to solar illumination for 30 min in ambient. (c) Zoomed-in plot of optical absorbance of a neat Y6 film from Fig. 3a of the main manuscript.

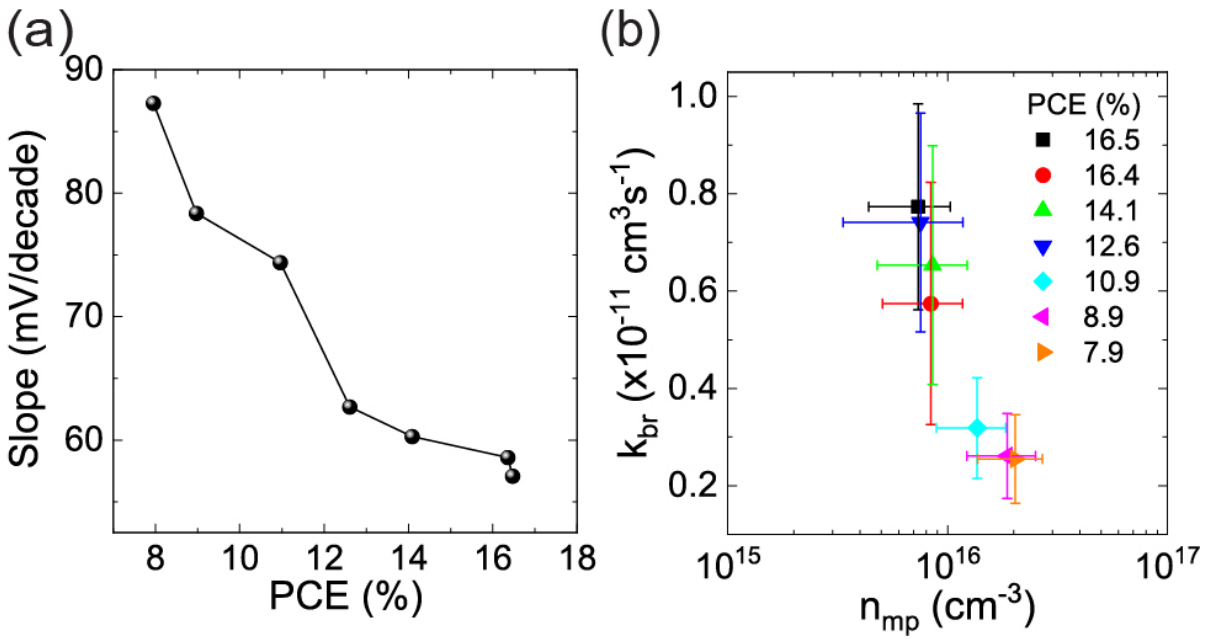

Figure S10. (a) A plot of the slope of V_{OC} versus log(I), where I is the illumination intensity, from Fig. 3b of the main text. (b) A plot of bimolecular recombination coefficient (k_{br}) vs n_{mp} at maximum power point extracted from IPDA at different stages of degradation corresponding to Fig. 3c.

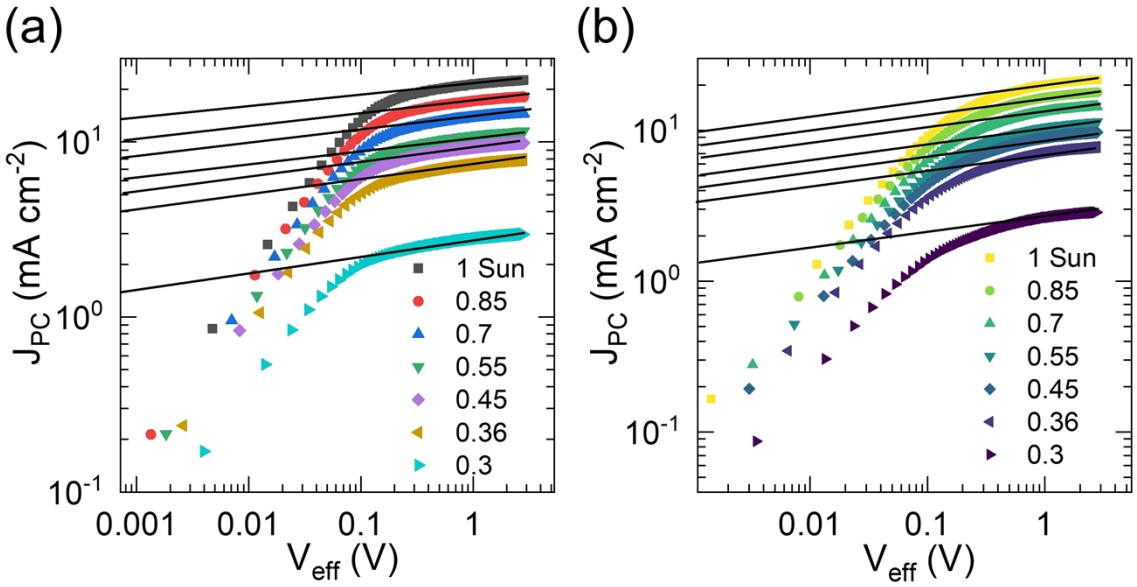

Figure S11. (a), (b) Plots of photocurrent (J_{PC}) versus effective voltage (V_{eff}) at varying illumination intensity for pristine (PCE = 14 %) and degraded (7.95 %) cells, respectively.

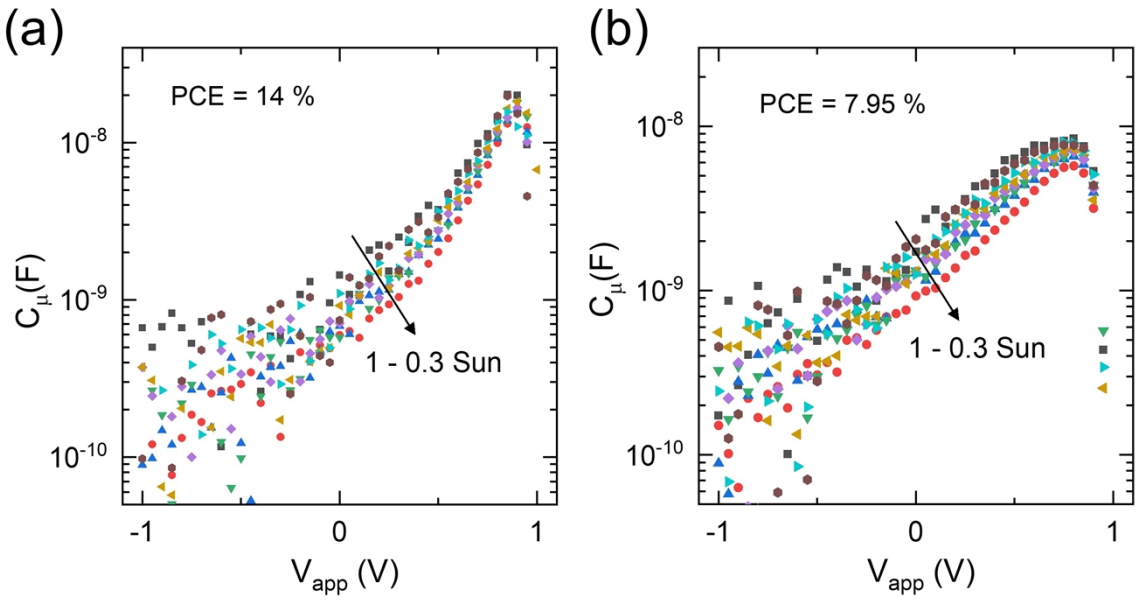

Figure S12. (a), (b) Plots of chemical capacitance (C_μ) versus applied voltage (V_{app}) at varying illumination intensity for pristine (PCE = 14%) and degraded (7.95 %) cells, respectively.

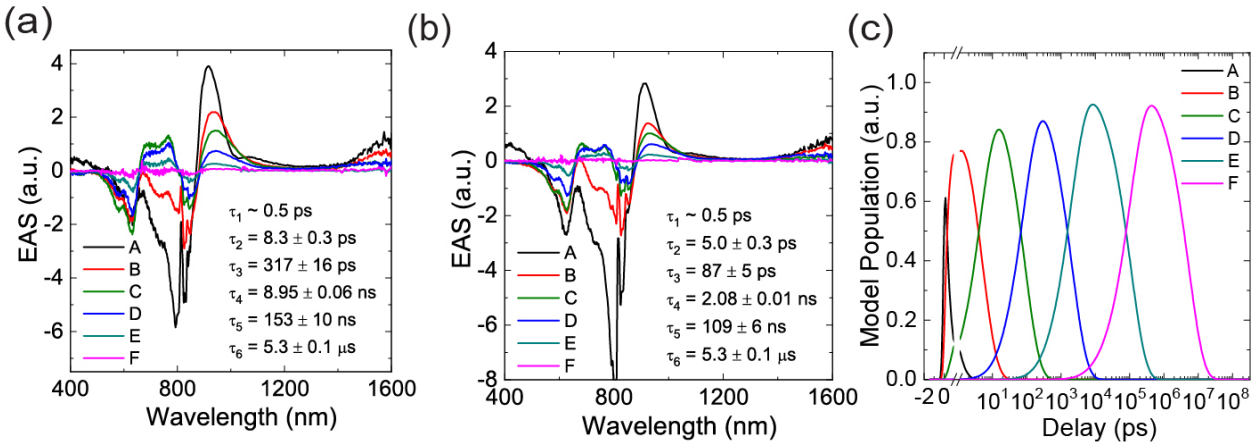

Figure S13. (a), (b) Evolution-associated spectra (EAS) of the pristine and degraded **PBDB-TF:Y6** blend film corresponding to global analyses fits shown in Fig. 4(b) and (e), respectively. Left insets in (a) and (b) denote different species while right insets show corresponding time constants from the model fit. (c) Model population dynamics of different species (A-F) for the degraded blend shown in (b).

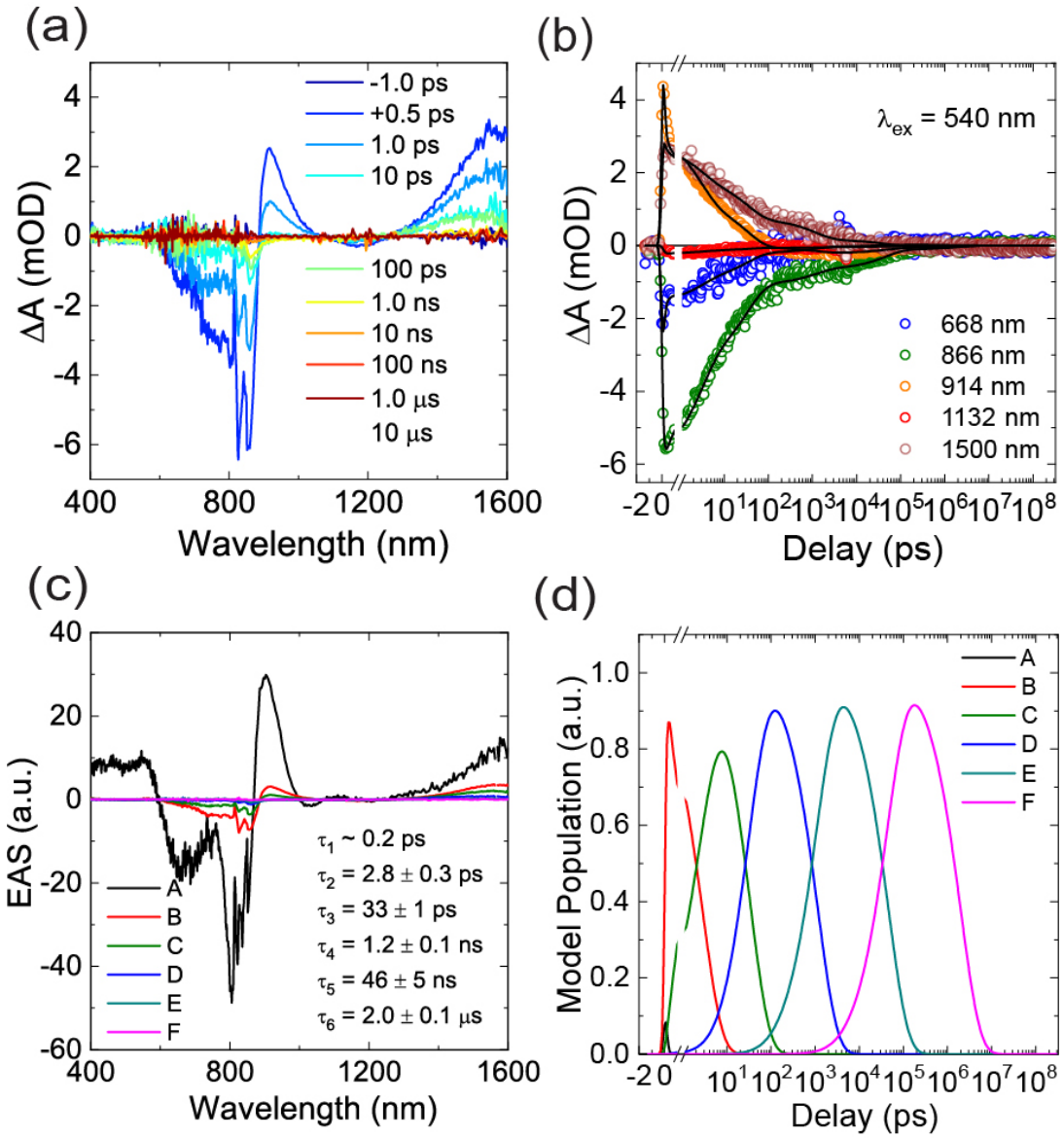

Figure S14. (a) TA spectra of a pristine **Y6** film taken at different delay times when excited at 540 nm. (b) Symbols show corresponding time-resolved differential absorption (ΔA) at indicated wavelengths while solid lines are fits to global analysis. (c) EAS spectra for the pristine **Y6** film corresponding to model fit in (b). The right inset shows time constants, $\tau_1 - \tau_6$ for different species, A-F, respectively. (d) Model population dynamics of species A-F in the pristine **Y6** film.

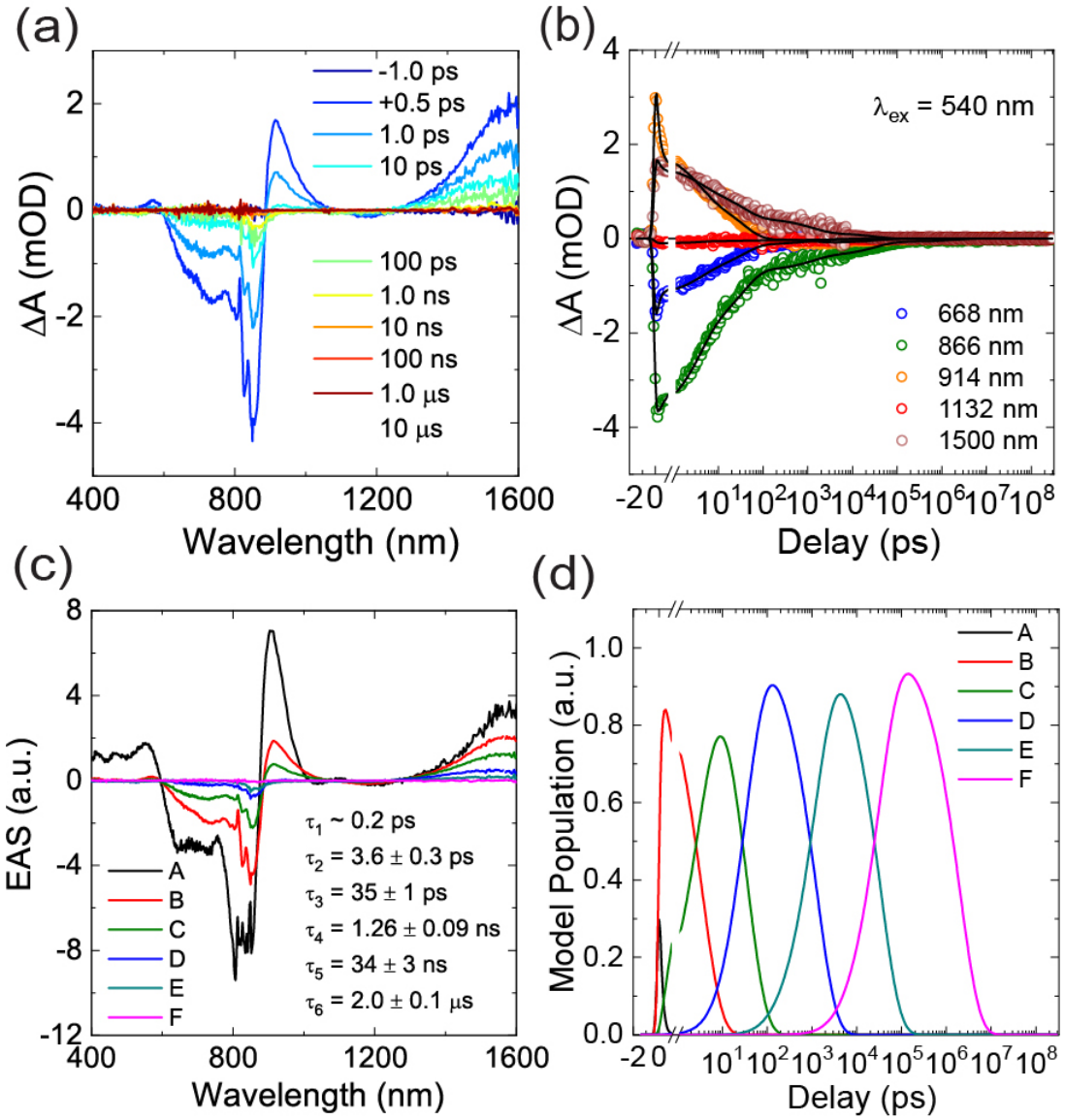

Figure S15. (a) TA spectra of the same **Y6** film from Fig. S14 after degradation taken at different delay times when excited at 540 nm. (b) Symbols show corresponding time-resolved ΔA at indicated wavelengths while solid lines show fits to global analysis. (c) EAS spectra for the degraded **Y6** film corresponding to model fit in (b). The right inset shows time constants, $\tau_1 - \tau_6$ for different species, A-F, respectively. (d) Model population dynamics of species A-F in the degraded **Y6** film.

Table S1. Time constants of different processes observed in the TA data extracted from model fitting for pristine and degraded **Y6** and **PBDB-TF:Y6** blend films.

	Pristine Y6	Degraded Y6	Pristine blend	Degraded blend
τ_1 (ps)	~0.3	~0.5	~0.5	~0.5
τ_2 (ps)	2.8 ± 0.3	5.0 ± 0.3	8.3 ± 0.3	5.0 ± 0.3
τ_3 (ps)	33 ± 1	35 ± 1	317 ± 16	87 ± 5
τ_4 (ns)	1.15 ± 0.01	1.2 ± 0.1	8.95 ± 0.06	2.08 ± 0.01
τ_5 (ns)	46 ± 5	34 ± 3	153 ± 10	109 ± 6
τ_6 (μs)	~2.0 ± 0.1	~2.0 ± 0.1	~5.3 ± 0.1	~5.3 ± 0.1

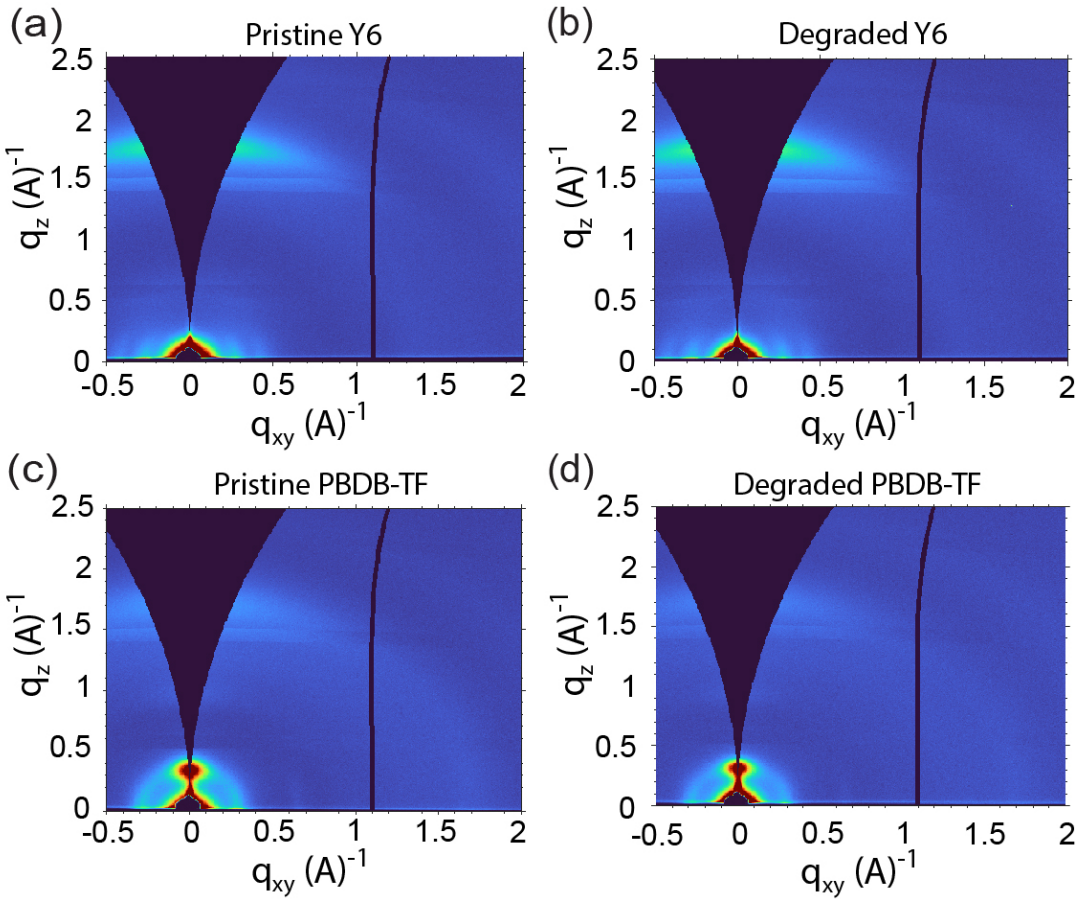

Figure S16. (a) – (d) GIWAXS plots of pristine and degraded pure **Y6** and **PBDB-TF** films, respectively.

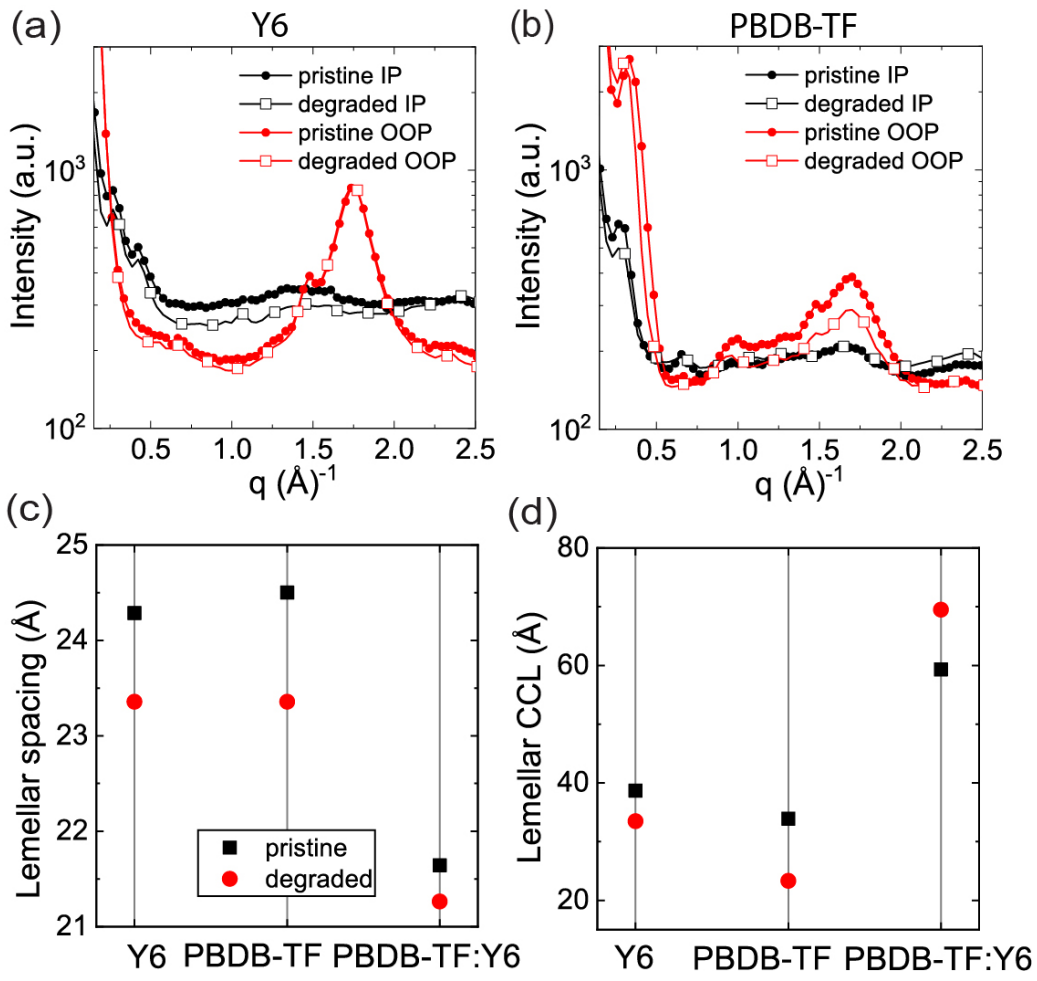

Figure S17. GIWAXS data line cuts (a,b) and extracted lamellar spacing and lamellar CCL and lamellar spacing parameters (c,d) for **Y6**, **PBDB-TF**, and **PBDB-TF:Y6** blend films.

Table S2. Model fit parameters from GIWAXS data for the pristine and degraded **PBDB-TF**, **Y6**, and **PBDB-TF:Y6** blend films.

Film	In-Plane (100)				Out-of-plane (010)			
	q_{xy}	d-spacing	FWHM	CCL	q_z	π-π distance	FWHM	CCL
	($Å^{-1}$)	(Å)	($Å^{-1}$)	(Å)	($Å^{-1}$)	(Å)	($Å^{-1}$)	(Å)
Pristine PBDB-TF	0.256	24.50	0.172	33.92	1.687	3.72	0.321	18.18
Pristine Y6	0.259	24.29	0.151	38.67	1.75	3.60	0.228	25.66
Pristine PBDB-TF:Y6	0.290	21.64	0.099	59.32	1.73	3.63	0.281	20.74
Degraded PBDB-TF	0.269	23.36	0.142	41.21	1.68	3.73	0.323	18.07
Degraded Y6	0.268	23.42	0.174	33.49	1.74	3.61	0.229	25.50
Degraded PBDB-TF:Y6	0.296	21.26	0.084	69.53	1.74	3.61	0.301	19.37

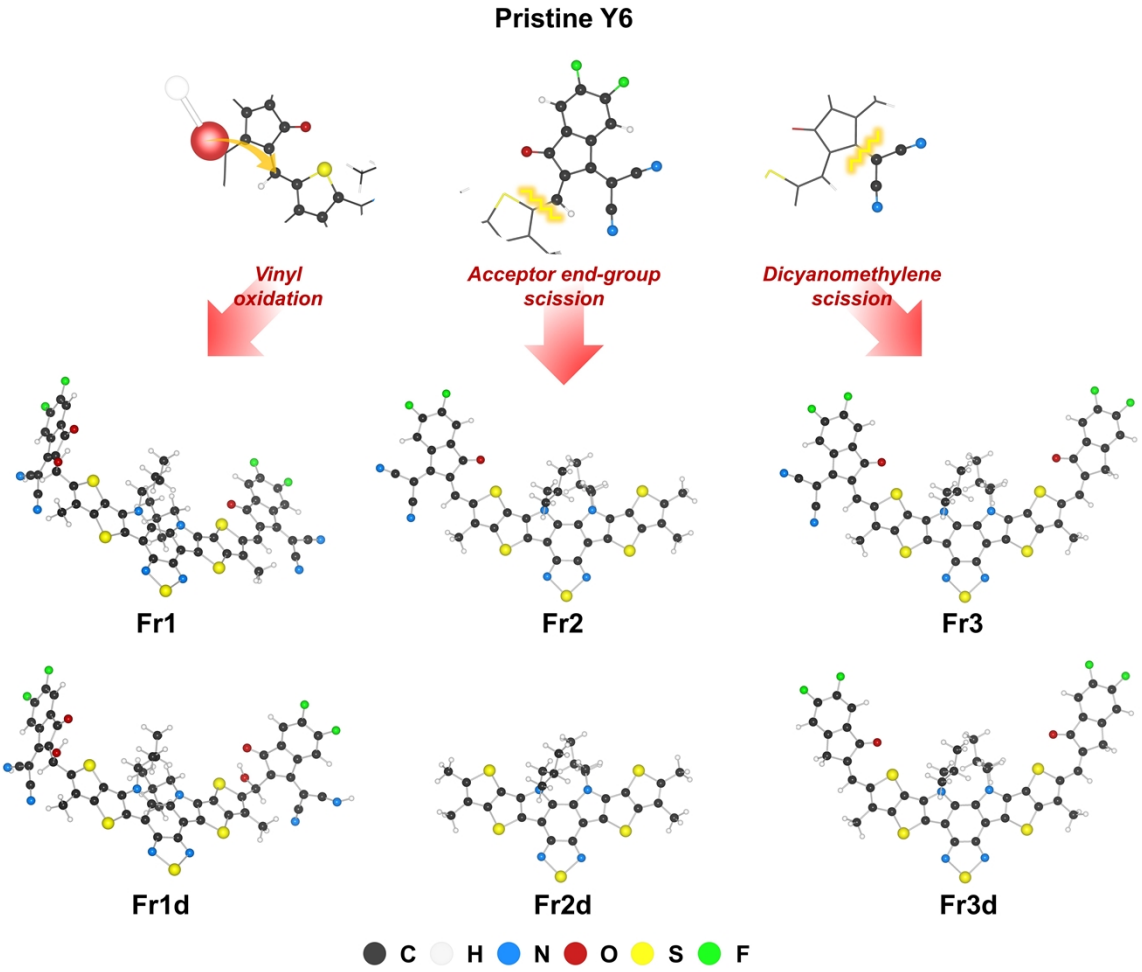

Figure S18. Optimized molecular structures of pristine **Y6** molecules and products after three kinds of degradation of **Y6**. Single degradation is considered in **Fr1**, **Fr2**, and **Fr3**, and double degradation is considered in **Fr1d**, **Fr2d**, and **Fr3d**, respectively. To achieve a neutral charge on each species, hydrogenation was done on the nitrogen atom within the dicyanomethylene group for **Fr1** and **Fr1d**, on the terminal carbon atom through end-group scission for **Fr2** and **Fr2d**, and on the terminal carbon atom resulting from dicyanomethylene scission for **Fr3** and **Fr3d**. Carbon, hydrogen, nitrogen, oxygen, sulfur, and fluorine are colored as black, white, blue, red, yellow, and neon green, respectively.

Table S3. Energy levels of frontier molecular orbitals in each **Y6**. Original pristine **Y6** refers to the full **Y6** molecule, as shown in Ref.[1] and Pristine **Y6** refers to a truncated **Y6** molecule to facilitate fast computations, as described in Section 8.

	Energy level (eV)			
	HOMO-1	*HOMO*	*LUMO*	*LUMO+1*
Original pristine **Y6**[1]	-5.93	-5.51	-4.29	-4.14
Pristine **Y6**	-5.88	-5.47	-4.24	-4.09

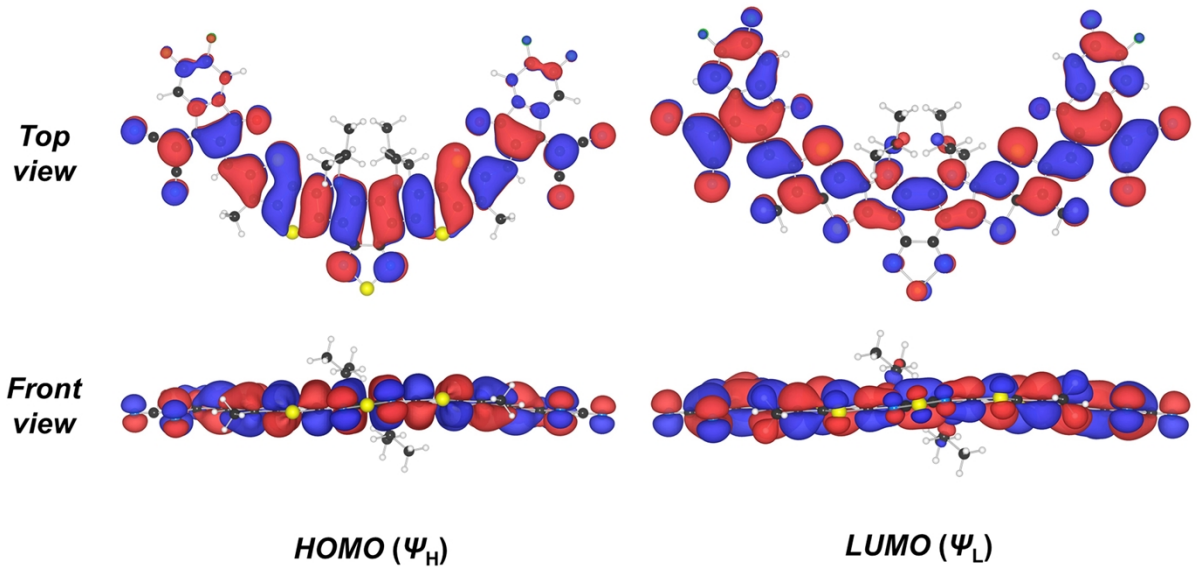

Figure S19. HOMO and LUMO of pristine **Y6** molecule. The color scheme on each element is identical to Fig. S18.

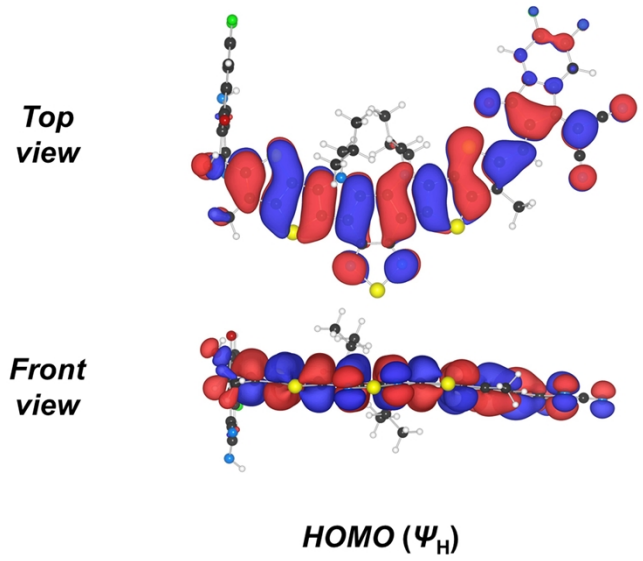

Figure S20. HOMO of **Fr1**. LUMO of **Fr1** is shown in Fig. 8a of the main text. The color scheme on each element is identical to Fig. S18.

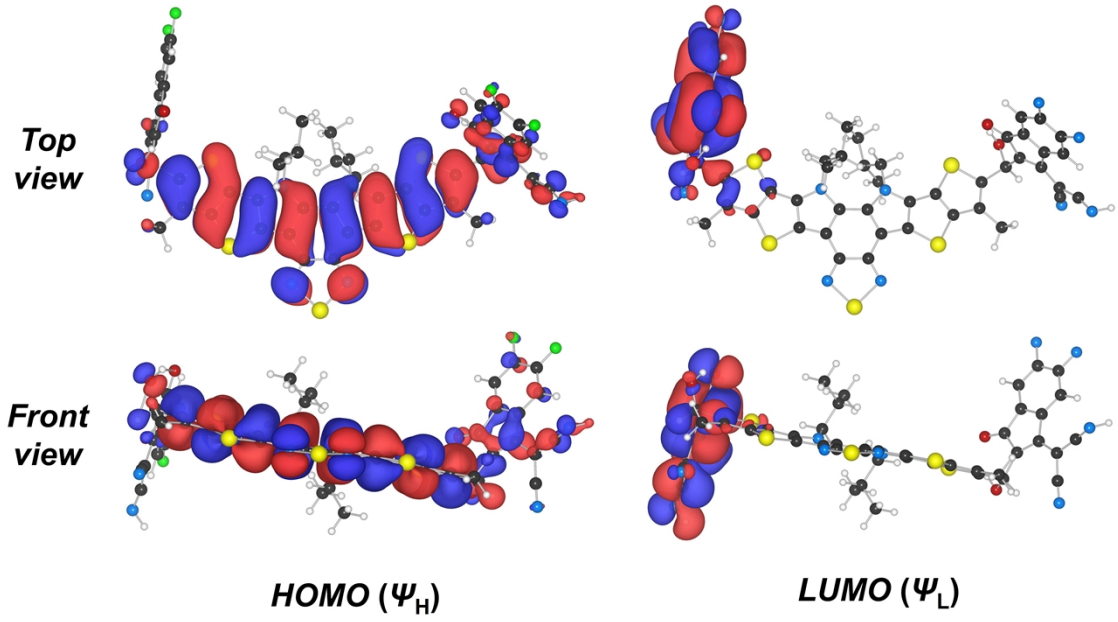

Figure S21. HOMO and LUMO of **Fr1d**. The color scheme on each element is identical to Fig. S18.

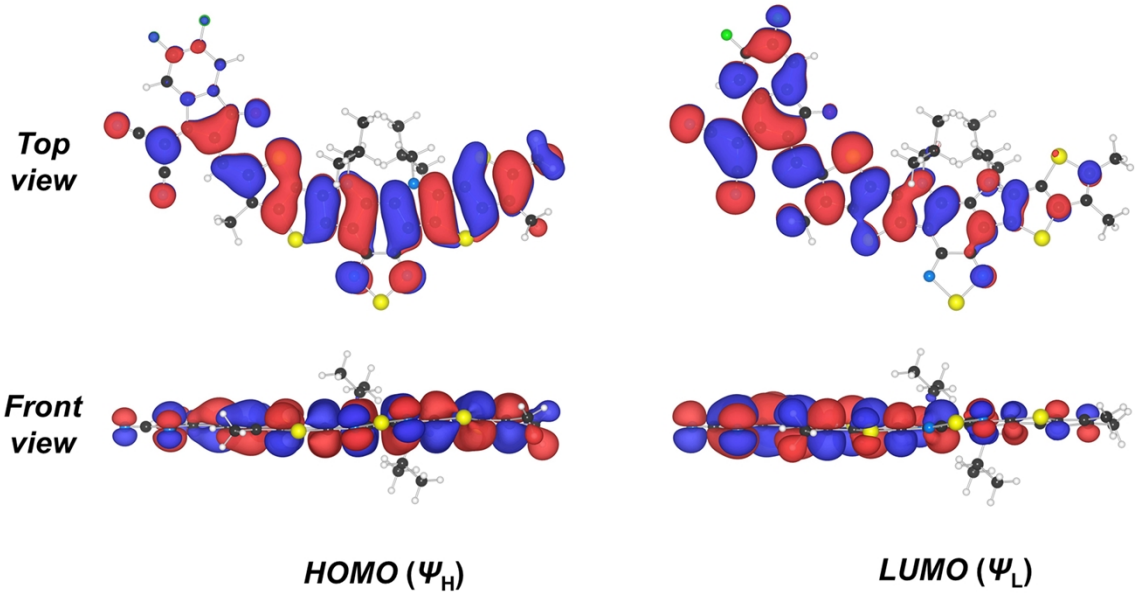

Figure S22. HOMO and LUMO of **Fr2**. The color scheme on each element is identical to Fig. S18.

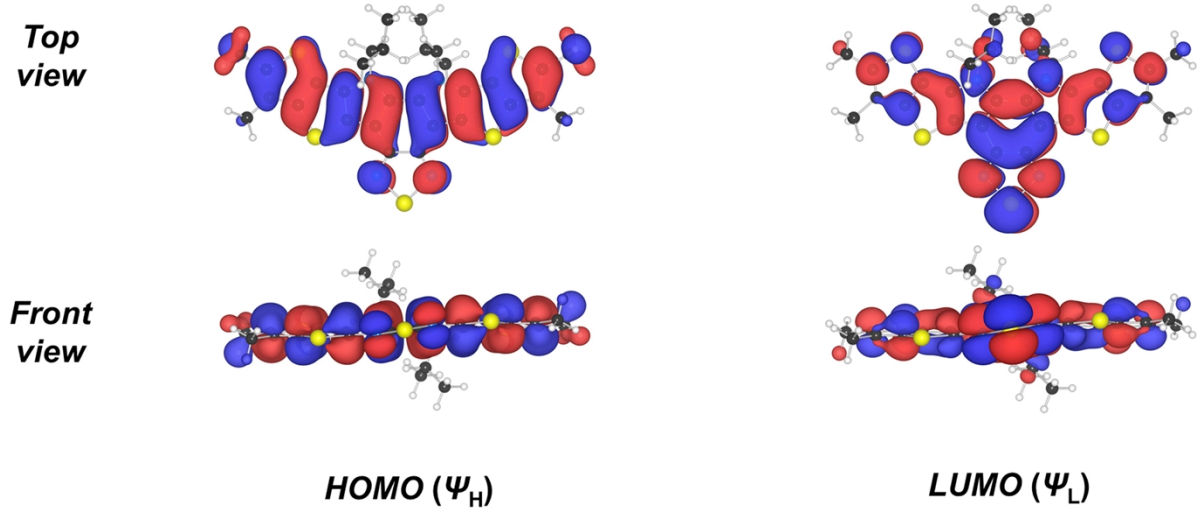

Figure S23. HOMO and LUMO of **Fr2d**. The color scheme on each element is identical to Fig. S18.

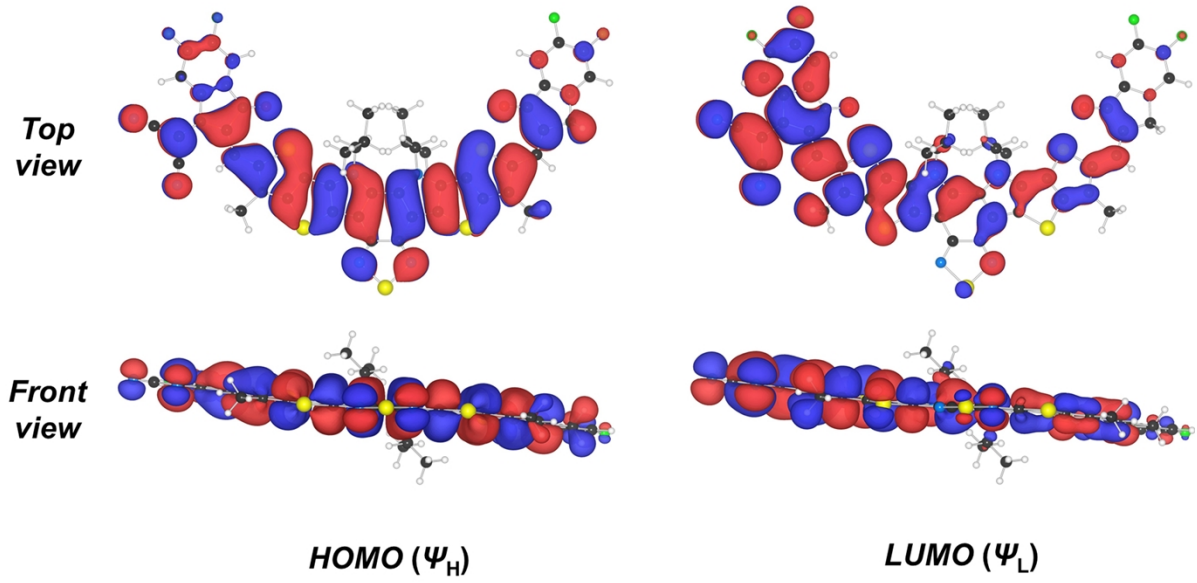

Figure S24. HOMO and LUMO of **Fr3**. The color scheme on each element is identical to Fig. S18.

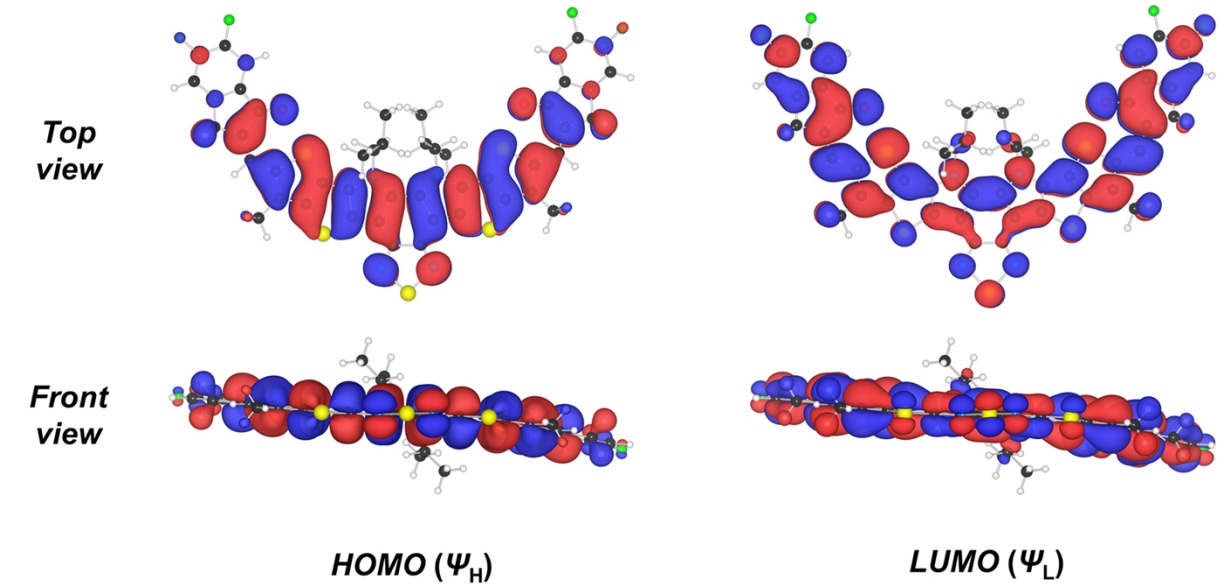

Figure S25. HOMO and LUMO of **Fr3d**. The color scheme on each element is identical to Fig. S18.

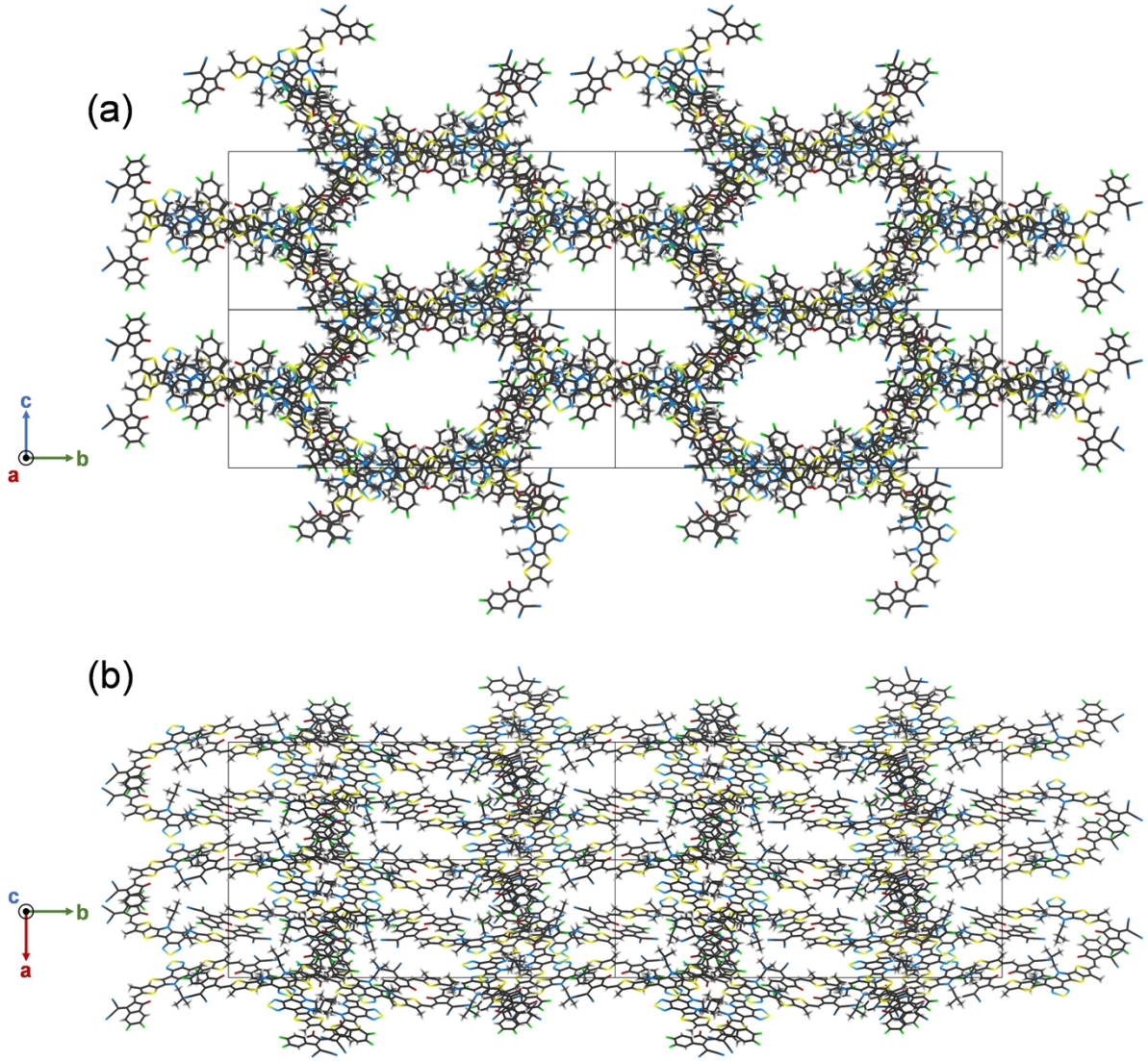

Figure S26. Optimized crystal structure of **Y6** in top and side views with the illustration of repeating unit cells, respectively. The color scheme on each element is identical to Fig. S18.

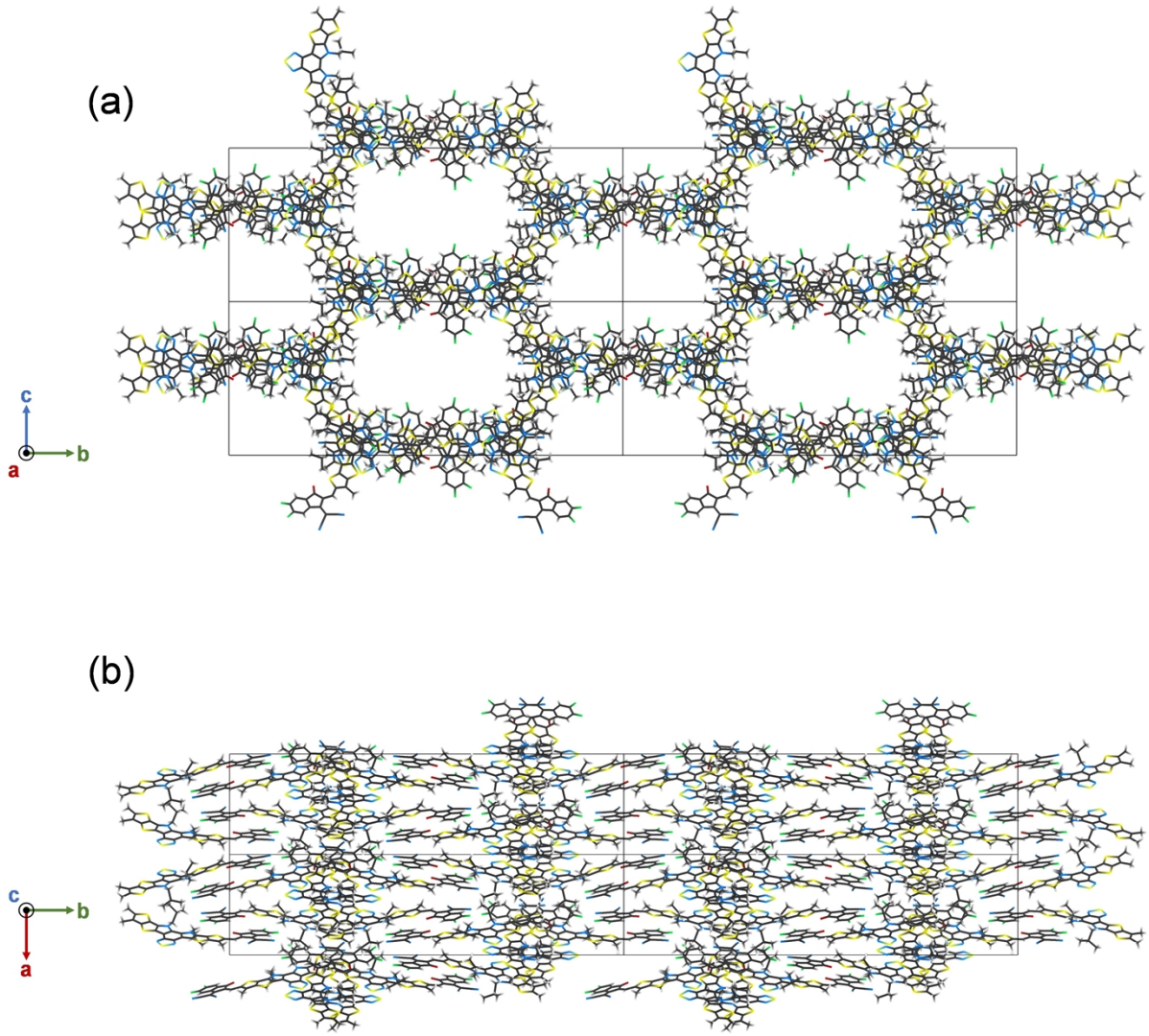

Figure S27. Optimized crystal structure of **Fr2** in top and side views with the illustration of repeating unit cells, respectively. The color scheme on each element is identical to Fig. S18.

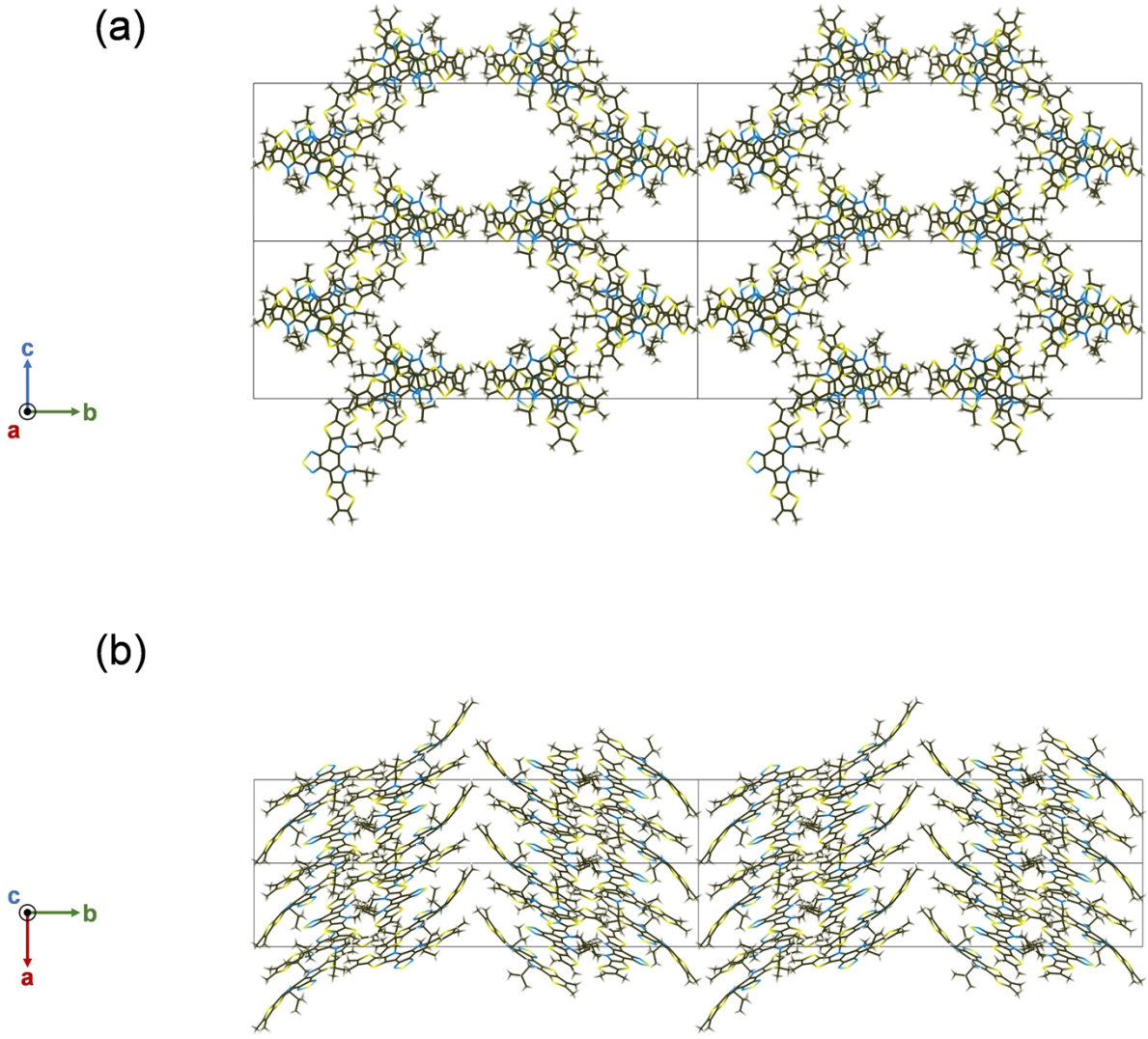

Figure S28. Optimized crystal structure of **Fr2d** in top and side views with the illustration of repeating unit cells, respectively. The color scheme on each element is identical to Fig. S18.

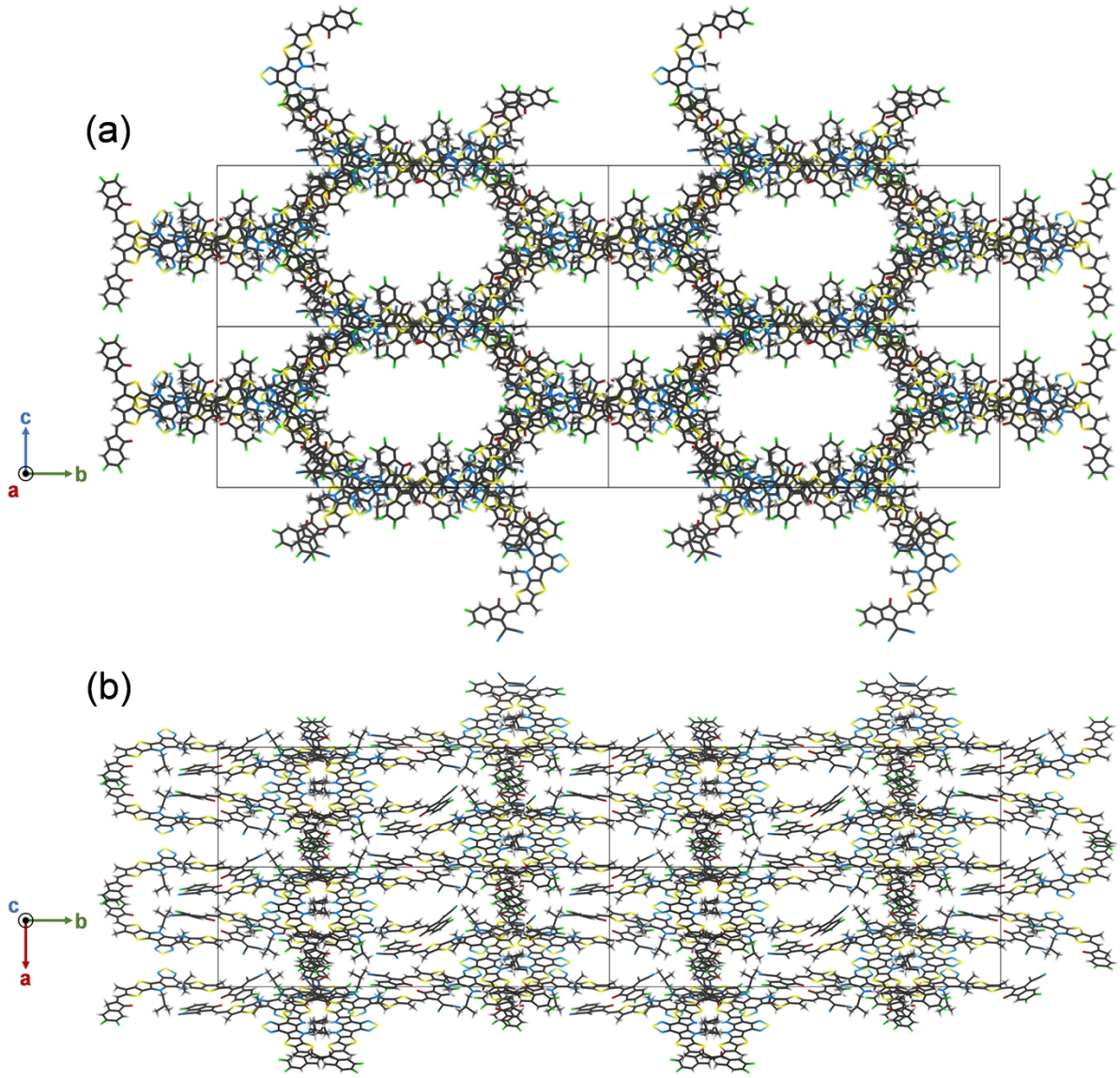

Figure S29. Optimized crystal structure of **Fr3** in top and side views with the illustration of repeating unit cells, respectively. The color scheme on each element is identical to Fig. S18.

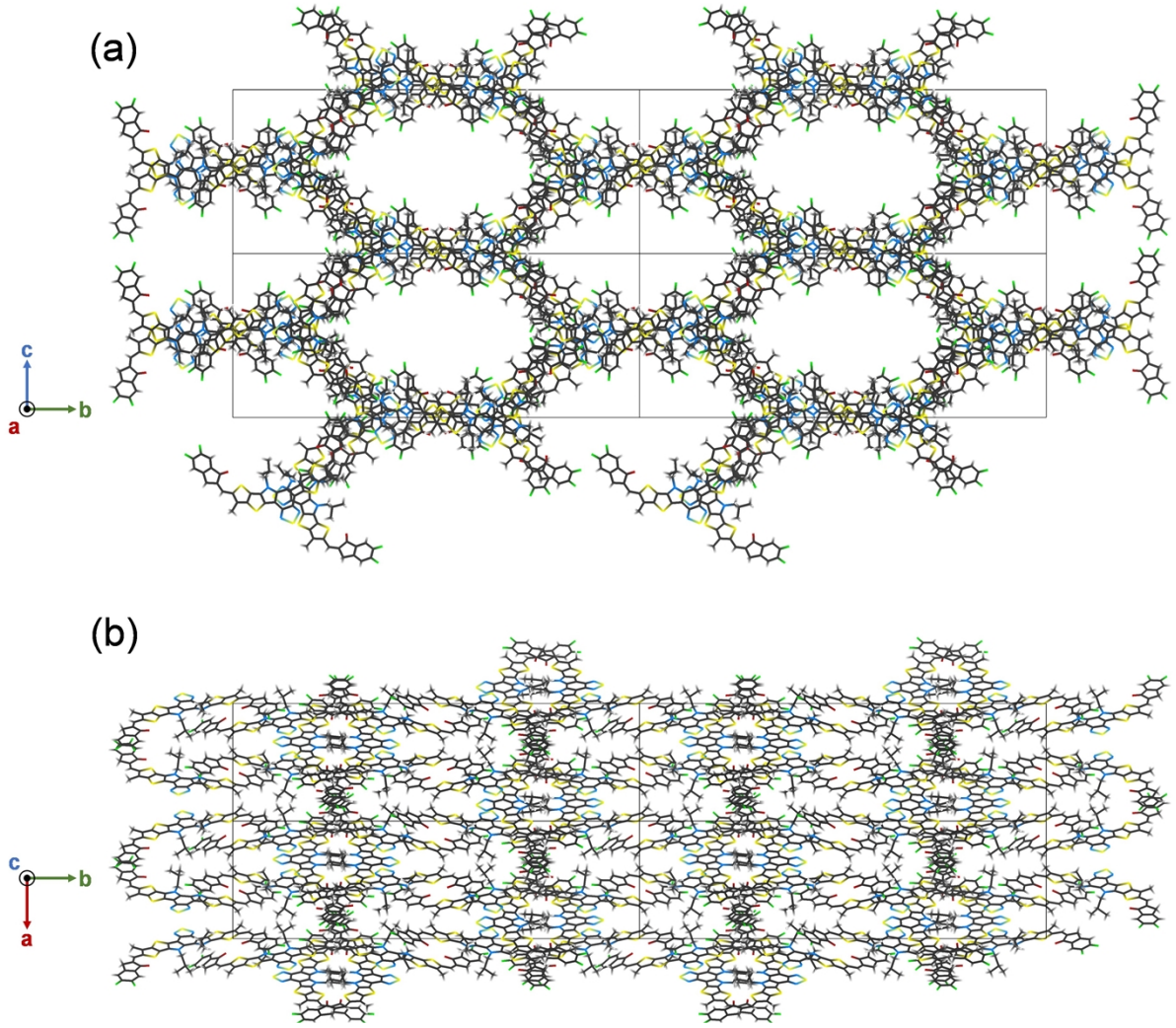

Figure S30. Optimized crystal structure of **Fr3d** in top and side views with the illustration of repeating unit cells, respectively. The color scheme on each element is identical to Fig. S18.

Table S4. Lattice parameters of **Y6** and products after five kinds of degradation on **Y6**. Note, **Fr1d** is excluded because it is not stable in crystal.

	a (Å)	b (Å)	c (Å)	α (°)	β (°)	γ (°)
Y6 ($C_{648}H_{360}N_{96}O_{24}F_{48}S_{60}$)	17.22	56.11	23.14	90.00	97.97	90.00
Fr1 ($C_{648}H_{384}N_{96}O_{36}F_{48}S_{60}$)	17.65	56.20	23.50	90.00	97.64	90.00
Fr2 ($C_{504}H_{360}N_{72}O_{12}F_{24}S_{60}$)	14.28	55.30	21.85	90.00	99.80	90.00
Fr2d ($C_{360}H_{360}N_{48}S_{60}$)	10.85	56.81	20.51	90.00	100.82	90.00
Fr3 ($C_{612}H_{384}N_{72}O_{24}F_{48}S_{60}$)	17.31	56.16	23.27	90.00	97.81	90.00
Fr3d ($C_{576}H_{408}N_{48}O_{24}F_{48}S_{60}$)	16.30	55.84	22.72	90.00	98.46	90.00

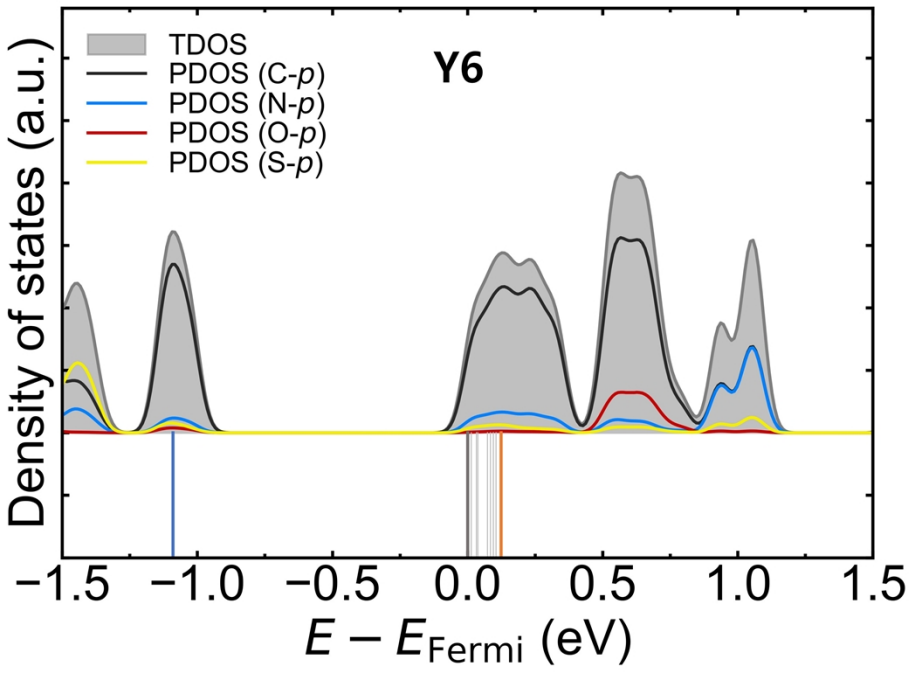

Figure S31. TDOS and PDOS (*p* orbital of carbon, nitrogen, oxygen, and sulfur) of **Y6** crystal structure. Energy levels of HOMO (E_{HOMO}), LUMO (E_{LUMO}), and trap energy (E_{Trap} = 0.12 eV) levels are shown by blue, orange, and grey solid vertical lines below the x-axis.

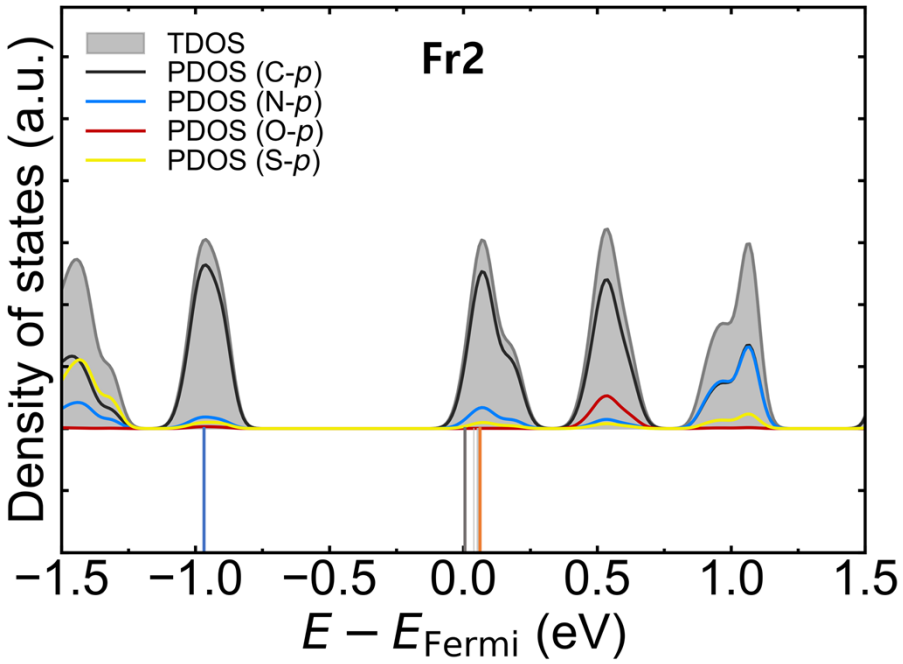

Figure S32. TDOS and PDOS (*p* orbital of carbon, nitrogen, oxygen, and sulfur) of **Fr2** crystal structure. Energy levels of HOMO (E_{HOMO}), LUMO (E_{LUMO}), and trap energy (E_{Trap} = 0.06 eV) levels are shown by blue, orange, and grey solid vertical lines below the x-axis.

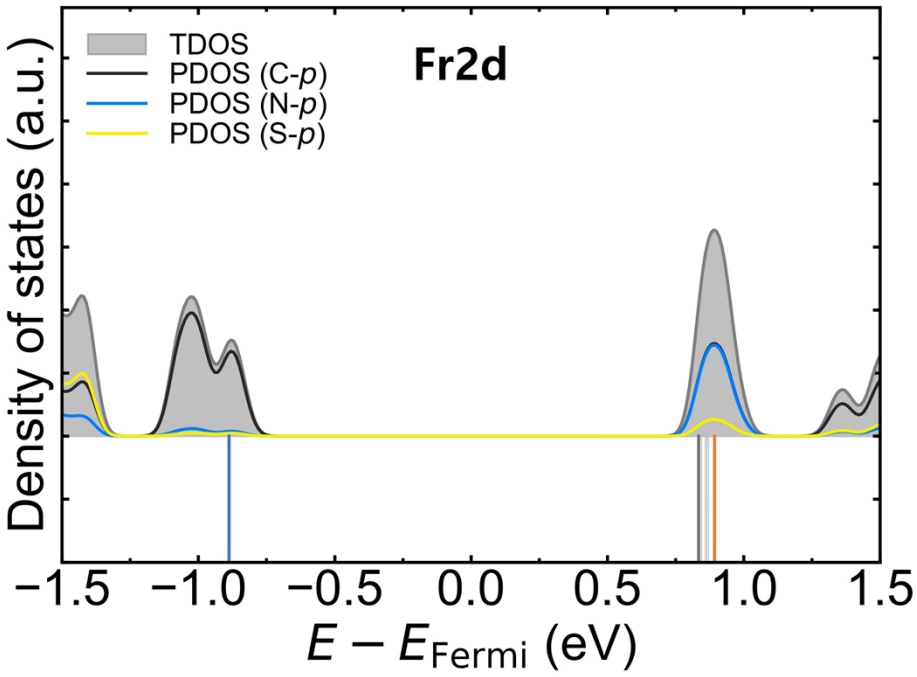

Figure S33. TDOS and PDOS (*p* orbital of carbon, nitrogen, oxygen, and sulfur) of **Fr2d** crystal structure. Energy levels of HOMO (E_{HOMO}), LUMO (E_{LUMO}), and trap energy (E_{Trap} = 0.06 eV) levels are shown by blue, orange, and grey solid vertical lines below the x-axis.

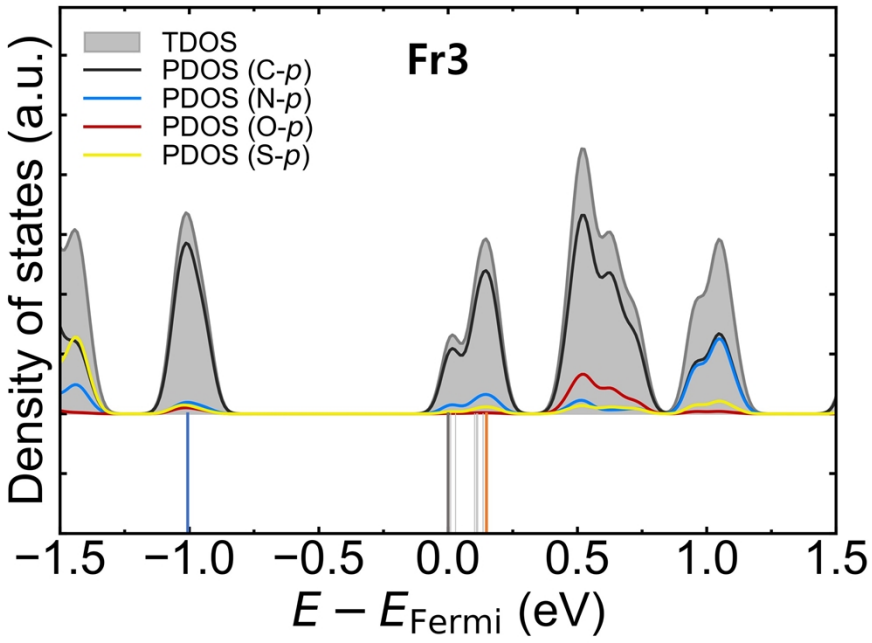

Figure S34. TDOS and PDOS (*p* orbital of carbon, nitrogen, oxygen, and sulfur) of **Fr3** crystal structure. Energy levels of HOMO (E_{HOMO}), LUMO (E_{LUMO}), and trap energy (E_{Trap} = 0.15 eV) levels are shown by blue, orange, and grey solid vertical lines below the x-axis.

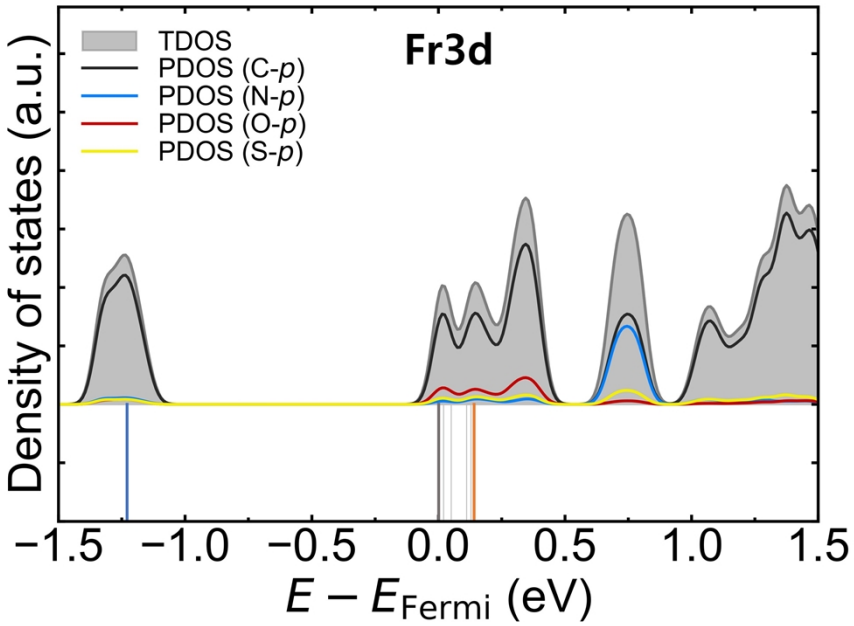

Figure S35. TDOS and PDOS (*p* orbital of carbon, nitrogen, oxygen, and sulfur) of **Fr3d** crystal structure. Energy levels of HOMO (E_{HOMO}), LUMO (E_{LUMO}), and trap energy (E_{Trap} = 0.12 eV) levels are shown by blue, orange, and grey solid vertical lines below the x-axis.

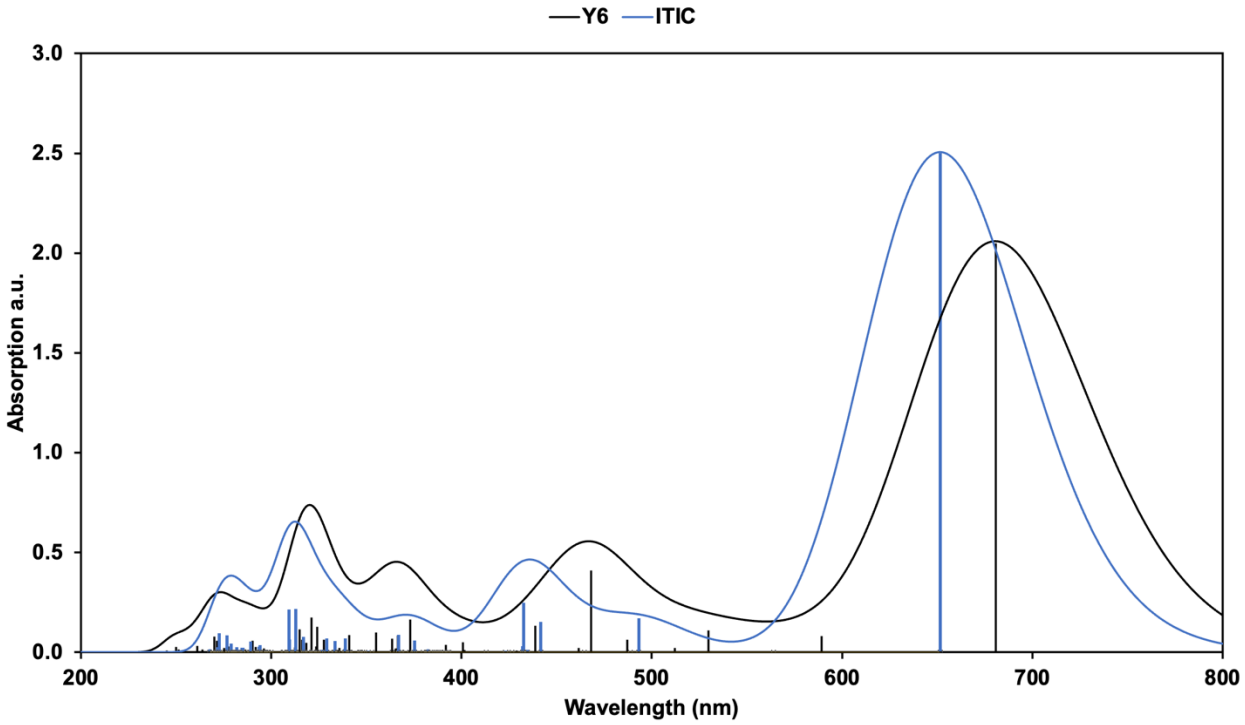

Figure S36. Computed UV/vis gas-phase spectrum for **Y6** and **ITIC** NFAs. **Y6** has a greater number of absorbing states in the 360 nm area of the spectrum compared to **ITIC**.

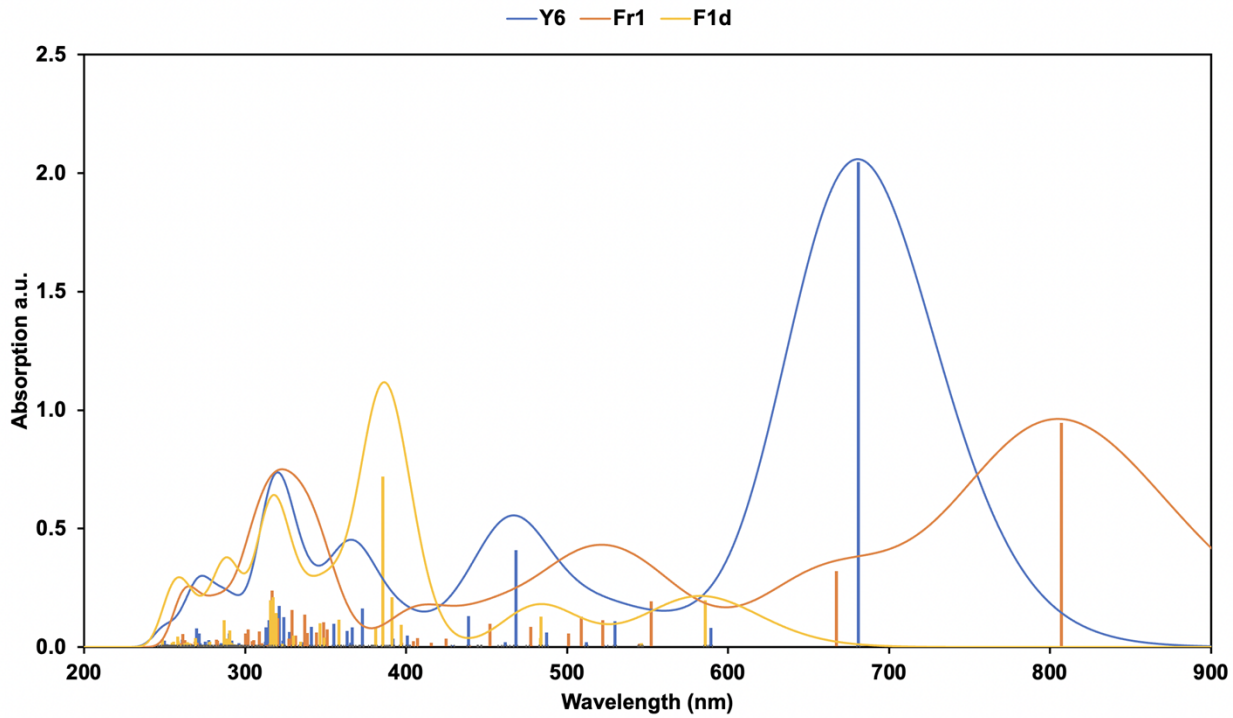

Figure S37. Computed UV/vis spectrum for **Y6** and oxidized vinyl group (**Fr1**). For comparison, we show the spectrum for both the doubly oxidized vinyl group (**Fr1d;** light orange) and the singly oxidized vinyl group (**Fr1**; dark orange), but we analyzed, both solid-state and gas-phase, only the singly oxidized fragment.

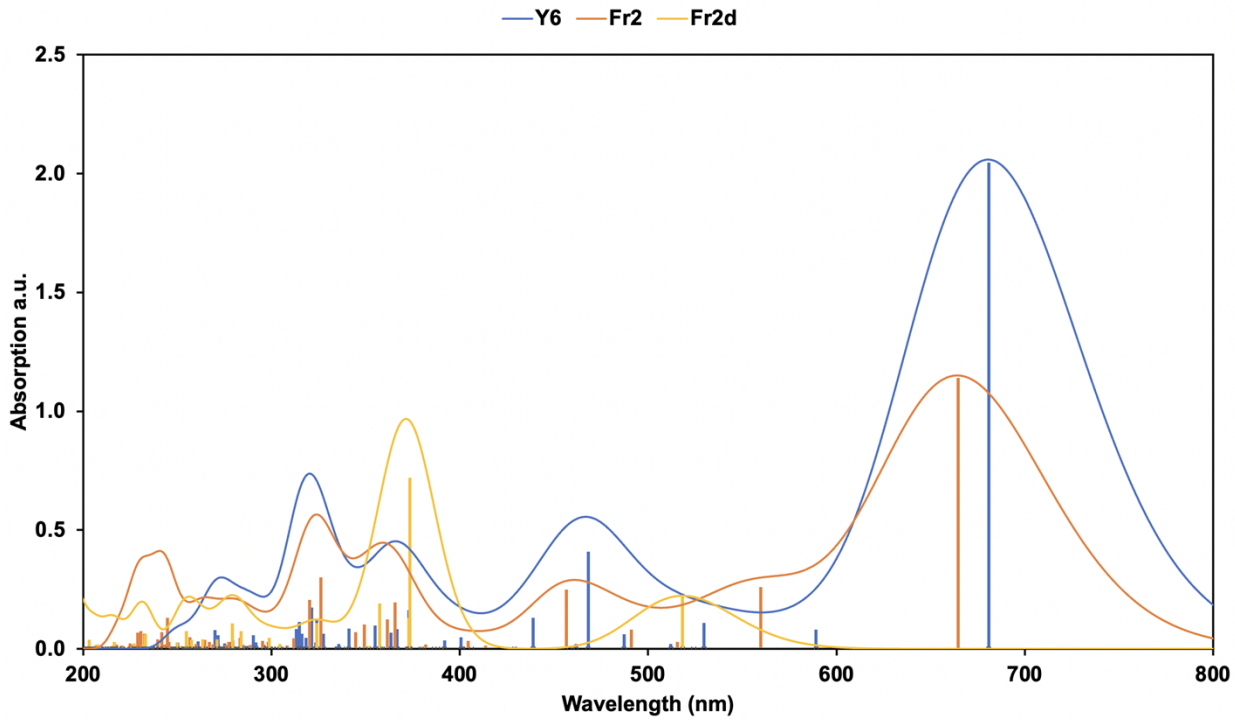

Figure S38. Computed UV/vis spectrum for **Y6** and acceptor scission (**Fr2**). For comparison, we show the spectrum for both acceptors missing (**Fr2d**; light orange) and with a single acceptor scission (**Fr2**; dark orange), but we analyzed, both solid-state and gas-phase, only the singly scissioned fragment.

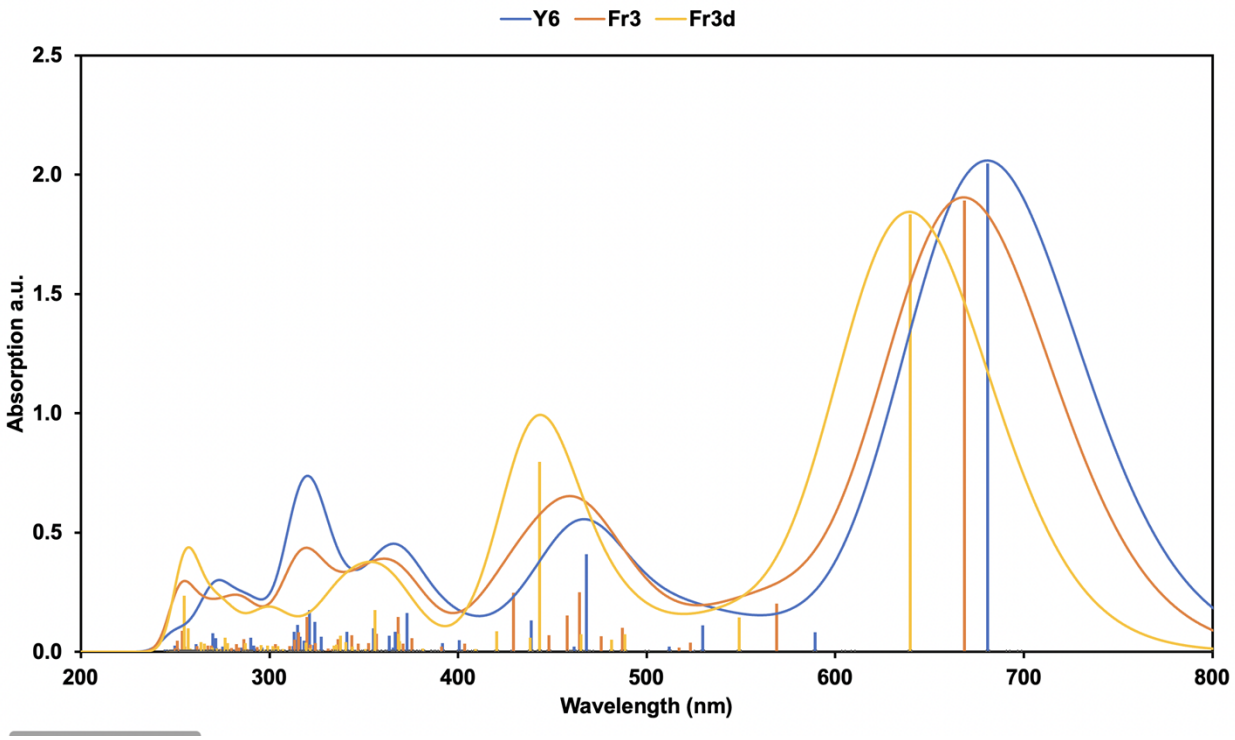

Figure S39. Computed UV/vis spectrum for **Y6** and dicyanomethylene scission (**Fr3**). For comparison, we show the spectrum for both dicyanomethylene groups missing (**Fr3d**; light orange) and with a single dicyanomethylene scission (**Fr3;** dark orange), but we analyzed, both solid-state and gas-phase, only the singly scissioned fragment.

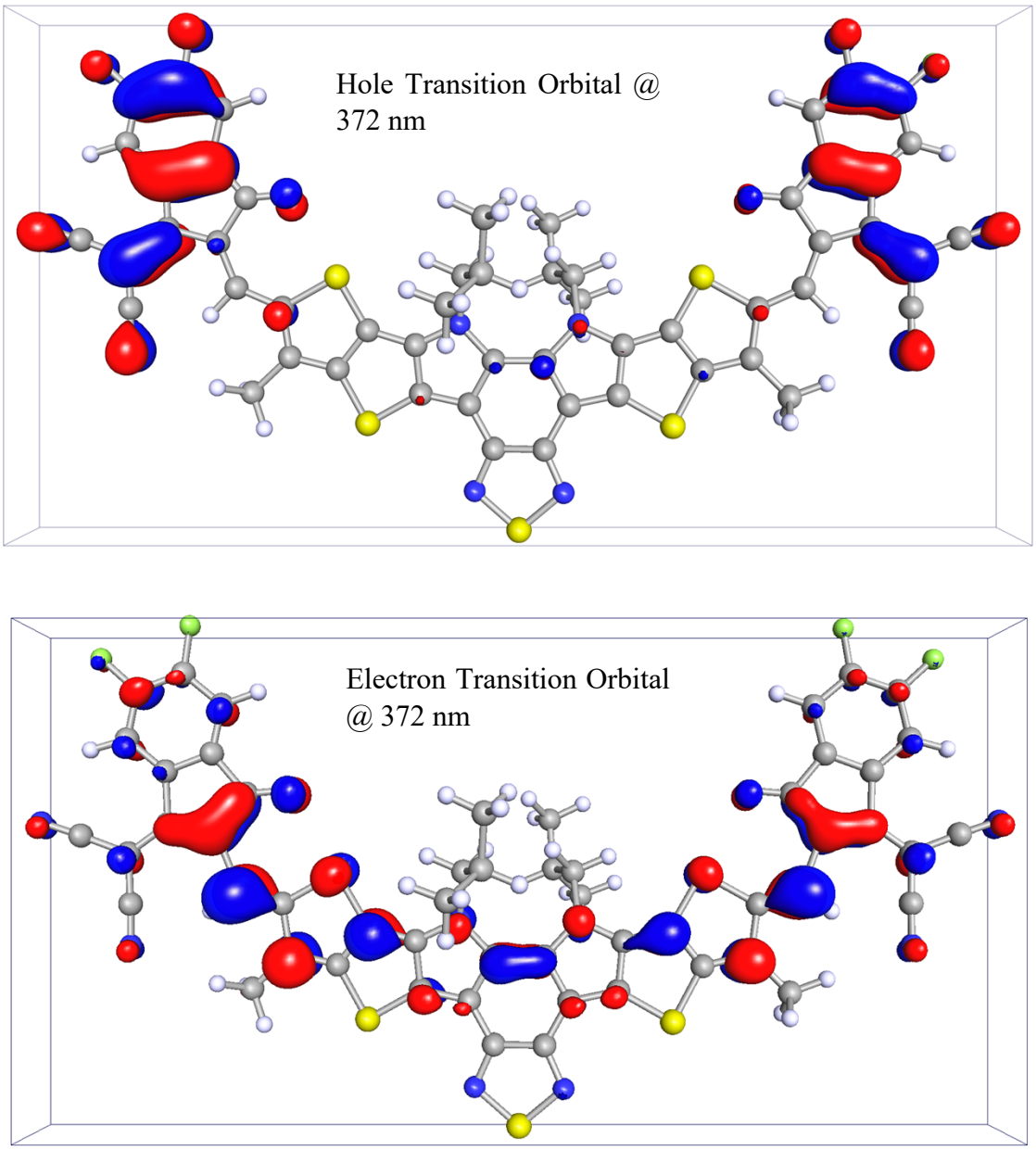

Figure S40. **Y6** NTO for excitation at 372 nm for the hole (top) and the electron (bottom) orbitals. The electron density is pulled away from the vinyl group.

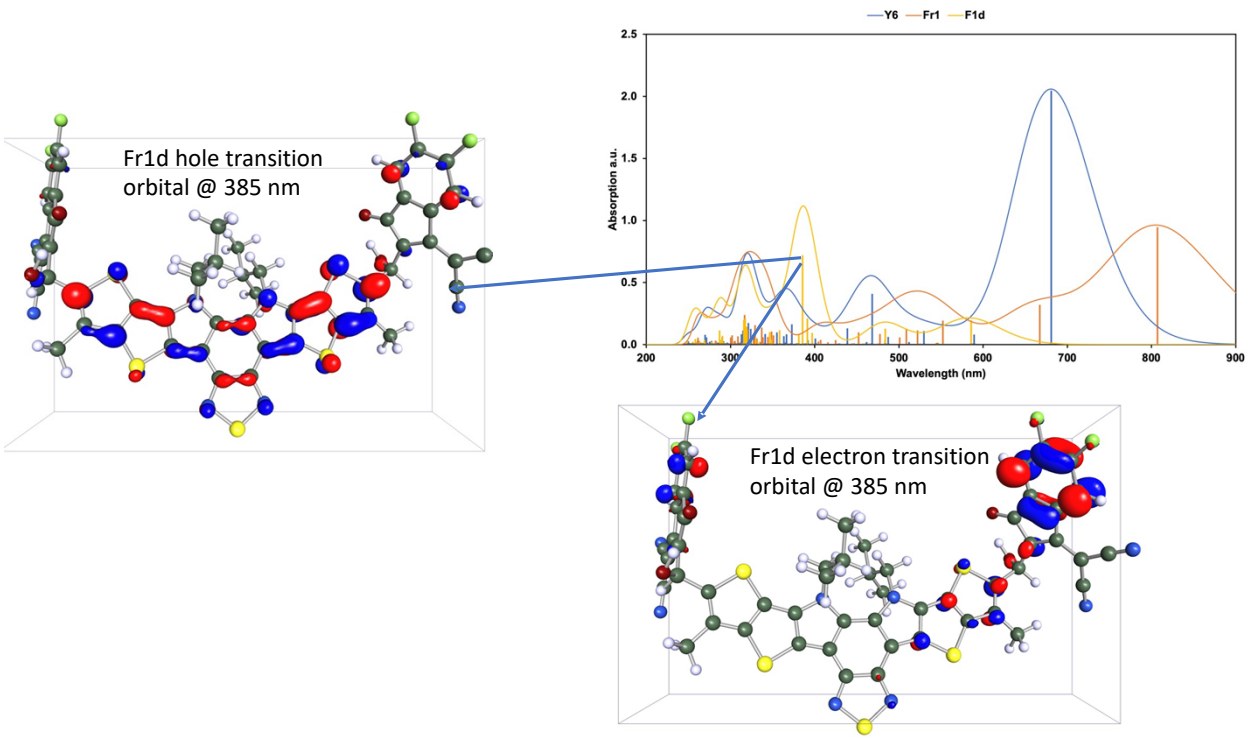

Figure S41. **Fr1d** NTOs at 385 nm embedded with UV/vis spectra (Fig. S37). Hole and electron NTOs give examples of an excited state that pulls electron density away from the vinyl group.

Table S5. Calculated m/z values for species resulting from different degradation pathways.

Molecule	m/z
Y6	1450.5
Y6'	1354.5
Fr1	1467.5
Fr1d	742.3
Fr2	1224.5
Fr2d	998.6
Fr3	1388.6
Fr3d	1326.6

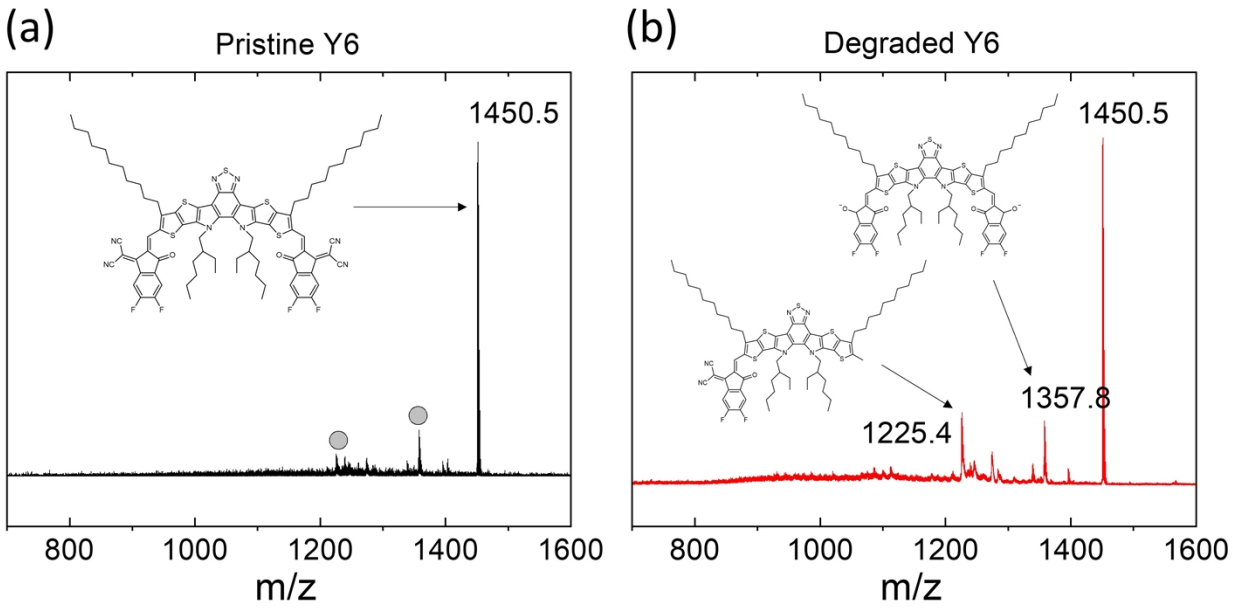

Figure S42. (a) MALDI-TOF mass spectrum of a pristine **Y6** film directly deposited on a stainless-steel plate. The dominant peak at 1450.5 corresponds to **Y6**. (b) MALDI-TOF mass spectrum of a degraded **Y6** film after solar illumination that was rinsed from ZnO/ITO substrate using 1,4-dichlorobenzene onto MALDI-TOF plate for the measurements. Additional prominent peaks at 1225.4 and 1357.8 could be assigned to fragment **Fr2** and a **Y6'** synthetic impurity, respectively. These peaks are significantly smaller in the pristine **Y6** film and are shown by gray circles in (a).

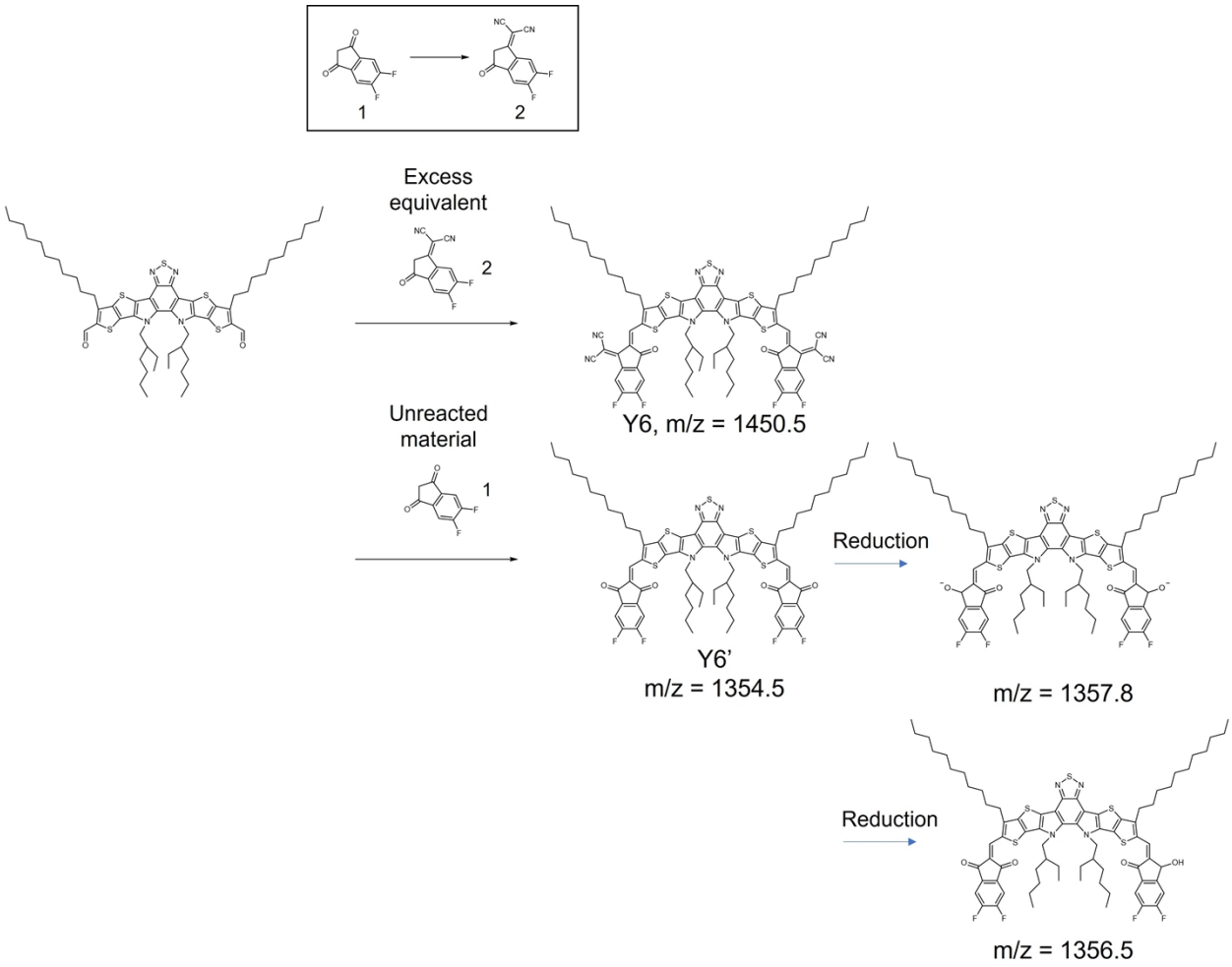

Figure S43. Chemical reactions involved in the synthesis of the **Y6** molecule. Unreacted compound (1) from the reaction in the box yields the **Y6'** molecule that can undergo further reduction reactions to produce molecules with m/z values of 1357.8 and 1365.5.

REFERENCES

1. G. Li, X. Zhang, L. O. Jones, J. M. Alzola, S. Mukherjee, L.-w. Feng, W. Zhu, C. L. Stern, W. Huang, J. Yu, V. K. Sangwan, D. M. DeLongchamp, K. L. Kohlstedt, M. R. Wasielewski, M. C. Hersam, G. C. Schatz, A. Facchetti and T. J. Marks, *Journal of the American Chemical Society*, 2021, **143**, 6123-6139.
2. G. Li, L.-W. Feng, S. Mukherjee, L. O. Jones, R. M. Jacobberger, W. Huang, R. M. Young, R. M. Pankow, W. Zhu, N. Lu, K. L. Kohlstedt, V. K. Sangwan, M. R. Wasielewski, M. C. Hersam, G. C. Schatz, D. M. DeLongchamp, A. Facchetti and T. J. Marks, *Eng. Envion. Sci.*, 2022, **15**, 645-659.
3. X. Zhang, G. Li, S. Mukherjee, W. Huang, D. Zheng, L.-W. Feng, Y. Chen, J. Wu, V. K. Sangwan, M. C. Hersam, D. M. DeLongchamp, J. Yu, A. Facchetti and T. J. Marks, *Adv. Eng. Mater.*, 2022, **12**, 2102172.
4. W. Zhu, A. P. Spencer, S. Mukherjee, J. M. Alzola, V. K. Sangwan, S. H. Amsterdam, S. M. Swick, L. O. Jones, M. C. Heiber, A. A. Herzing, G. Li, C. L. Stern, D. M. DeLongchamp, K. L. Kohlstedt, M. C. Hersam, G. C. Schatz, M. R. Wasielewski, L. X. Chen, A. Facchetti and T. J. Marks, *Journal of the American Chemical Society*, 2020, **142**, 14532-14547.
5. M. C. Heiber, T. Okubo, S.-J. Ko, B. R. Luginbuhl, N. A. Ran, M. Wang, H. Wang, M. A. Uddin, H. Y. Woo, G. C. Bazan and T.-Q. Nguyen, *Eng. Envion. Sci.*, 2018, **11**, 3019-3032.
6. L.-W. Feng, J. Chen, S. Mukherjee, V. K. Sangwan, W. Huang, Y. Chen, D. Zheng, J. W. Strzalka, G. Wang, M. C. Hersam, D. DeLongchamp, A. Facchetti and T. J. Marks, *ACS Eng. Lett.*, 2020, **5**, 1780-1787.
7. R. M. Young, S. M. Dyar, J. C. Barnes, M. Juricek, J. F. Stoddart, D. T. Co and M. R. Wasielewski, *J. Phys. Chem. A*, 2013, **117**, 12438-12448.
8. B. Hourahine, B. Aradi, V. Blum, F. Bonafé, A. Buccheri, C. Camacho, C. Cevallos, M. Y. Deshaye, T. Dumitrică, A. Dominguez, S. Ehlert, M. Elstner, T. van der Heide, J. Hermann, S. Irle, J. J. Kranz, C. Köhler, T. Kowalczyk, T. Kubař, I. S. Lee, V. Lutsker, R. J. Maurer, S. K. Min, I. Mitchell, C. Negre, T. A. Niehaus, A. M. N. Niklasson, A. J. Page, A. Pecchia, G. Penazzi, M. P. Persson, J. Řezáč, C. G. Sánchez, M. Sternberg, M. Stöhr, F. Stuckenberg, A. Tkatchenko, V. W.-z. Yu and T. Frauenheim, *J. Chem. Phys.*, 2020, **152**, 124101.
9. M. Gaus, A. Goez and M. Elstner, *J Chem Theory Comput*, 2013, **9**, 338-354.
10. M. Gaus, X. Lu, M. Elstner and Q. Cui, *J Chem Theory Comput*, 2014, **10**, 1518-1537.
11. M. Kubillus, T. Kubař, M. Gaus, J. Řezáč and M. Elstner, *J Chem Theory Comput*, 2015, **11**, 332-342.
12. S. Grimme, J. Antony, S. Ehrlich and H. Krieg, *J. Chem. Phys.*, 2010, **132**, 154104.
13. S. Grimme, S. Ehrlich and L. Goerigk, *Journal of Computational Chemistry*, 2011, **32**, 1456-1465.
14. K. Momma and F. Izumi, *Journal of Applied Crystallography*, 2011, **44**, 1272-1276.
15. S. G. Balasubramani, G. P. Chen, S. Coriani, M. Diedenhofen, M. S. Frank, Y. J. Franzke, F. Furche, R. Grotjahn, M. E. Harding, C. Hättig, A. Hellweg, B. Helmich-Paris, C. Holzer, U. Huniar, M. Kaupp, A. Marefat Khah, S. Karbalaei Khani, T. Müller, F. Mack, B. D. Nguyen, S. M. Parker, E. Perlt, D. Rappoport, K. Reiter, S. Roy, M. Rückert, G. Schmitz, M. Sierka, E. Tapavicza, D. P. Tew, C. van Wüllen, V. K. Voora, F. Weigend, A. Wodyński and J. M. Yu, *J. Chem. Phys.*, 2020, **152**, 184107.
16. A. V. Luzanov, A. A. Sukhorukov and V. É. Umanskii, *Theoretical and Experimental Chemistry*, 1976, **10**, 354-361.